17 Convection of a Bingham Fluid in a Porous Medium

D. Andrew S. Rees

CONTENTS

17.1 INTRODUCTION

The chief purpose of this chapter is to consider convective flows of a Bingham fluid when it saturates a porous medium. My interest in this topic arose after seeing the work of Turan et al. (2012) at the *Advances in Computational Heat Transfer Symposium*, which was held at the University of Bath. In that paper, the authors considered the convection of a Bingham fluid in a square cavity heated from a vertical sidewall and cooled by the other. Plots of streamlines show unyielded regions where the local shear stress is less than the yield stress. I immediately wondered what the equivalent would be for a porous medium, and I started searching for papers on the topic. I was assisted in this work by a final year undergraduate who also worked on some network modeling aspects (Nash 2013). Of course, the presence of the solid matrix means that flow in a porous medium will happen only when the yield stress is exceeded locally. If one were, in the first instance, to think of a porous medium as a bundle of tubes or a collection of channels or even a network of channels, then

simple considerations of Poiseuille flow or Hagen–Poiseuille flow in these tubes or channels lead one immediately to realize that *unyielded* in the porous medium context actually means *no flow*. This is not necessarily the case for the so-called clear fluid flows, such as Poiseuille flow, where one may have flow within a channel, but the unyielded central portion still moves. Therefore, I have used the opportunity to provide this chapter as one where I would have an extra impetus to study the general topic of Bingham fluids and how they convect in a porous medium.

It has become apparent, at one and the same time, that (1) there is a huge literature associated with yield-stress fluids in general, one that I had no idea existed, and (2) there are very few papers indeed that deal with the convection of a yield-stress fluid in a porous medium even though there is much interest in isothermal flows in porous media. This juxtaposition of glut and famine has therefore guided how I have approached the task of writing. So this chapter begins with a brief, possibly too brief, introduction first to the concept of a yield-stress fluid in general, and second to the modeling of isothermal flows in porous media. There are some controversies that the reader, new to this topic, will, I hope, find useful to know. There are varieties of constituent models and even the questioning of whether there is indeed such a thing as a yield stress. My aim here is not to provide a definitive set of textbook information, but merely to indicate some of the issues that may usefully be pursued.

After a long time spent searching the published literature, I was successful in finding only about a dozen papers on the convection of a yield-stress fluid in a porous medium, and I was surprised to find that all of these are devoted to boundary-layer flows. There was nothing at all on convection in channels, on convection in cavities, or on the analog to the Darcy–Bénard problem. Therefore, much of this chapter concentrates on the new work on these topics and gives a flavor of what to expect in more detailed studies.

After introducing more fully the concept of a yield-stress fluid and of how it is modeled when flowing through a porous medium, the chapter continues with further new studies of isothermal flows in distributions of channels and in square networks. The latter allows the definition of a new type of Darcy–Bingham law for flow in such a structured medium and demonstrates that flow is anisotropic in periodic media. After that, we consider the flow which is induced in a sidewall-heated vertical channel, and it is possible to derive analytical solutions for this case. Nonlinear convection in sidewall-heated cavities are also computed, as are flows of Darcy–Bénard type; in both cases, certain qualitative features that are present for fluids without yield stresses are changed. An unsteady boundary-layer flow is also considered in some detail. Finally, the steady boundary-layer flows mentioned earlier are considered. In this case, we make an argument that there are some difficulties with the classical type of boundary-layer analysis where the subsequent consideration is not made of the flow that occurs in the outer external region. We show that, when the yield criterion lies within the boundary layer itself, then entrainment into the boundary, something that must happen (1) to provide fluid to replace that which is convected upward and (2) to prove a mechanism for restricting the conduction of heat perpendicularly away from the surface, cannot happen because it is too weak to overcome the yield criterion. Thus, this chapter provides a great deal of new information on new topics. It is not comprehensive but provides a foundation for more detailed studies, which I intend to pursue in the next few years.

17.2 YIELD-STRESS FLUIDS AND THEIR MODELING

In this section, we take a brief look at various models of Bingham fluids and how one might then define macroscopic laws for the flow of such fluids in porous media.

17.2.1 Bingham Fluids

A Bingham fluid is essentially a Newtonian fluid but one with a yield stress. Thus, the fluid flows only when a sufficiently large stress is imposed, but thereafter, it flows with a constant

viscosity. This is seen most easily for unidirectional flow where u is the velocity in the x-direction but is one that is a function of y. A one-dimensional Newtonian flow obeys the following stress/strain relationship:

$$\tau = \mu\dot{\gamma} = \mu\frac{du}{dy}, \tag{17.1}$$

where

τ is the shear stress

$\dot{\gamma}$ is the rate of strain

In terms of these quantities, the x-momentum equation for one-dimensional flow without buoyancy may be rewritten in the form

$$0 = -\frac{dp}{dx} + \frac{d\tau}{dy}. \tag{17.2}$$

A Bingham fluid has a yield stress which we notate as τ_0. The equivalent of (17.1) is

$$\begin{aligned} \tau > \tau_0 \quad &\Rightarrow \quad \mu\frac{du}{dy} = \tau - \tau_0, \\ -\tau_0 < \tau < \tau_0 \quad &\Rightarrow \quad \frac{du}{dy} = 0, \\ \tau < -\tau_0 \quad &\Rightarrow \quad \mu\frac{du}{dy} = \tau + \tau_0. \end{aligned} \tag{17.3}$$

It is the second equation in (17.3) that gives u = constant when the fluid is in its unyielded state. In such equations, the quantity, μ, is sometimes called the plastic viscosity (Denn and Bonn 2011).

It is worth mentioning that two of the many other commonly used models for yield-stress fluids are those describing Casson and Herschel–Bulkley fluids. If we were to summarize the Bingham properties given in (17.3) by

$$\tau = \tau_0 + \mu\dot{\gamma}, \tag{17.4}$$

where it is assumed that $\tau > \tau_0$, then a Casson fluid is given by

$$\sqrt{\tau} = \sqrt{\tau_0} + \sqrt{\mu\dot{\gamma}}, \tag{17.5}$$

or equivalently by

$$\tau = \tau_0 + \mu\dot{\gamma} + 2\sqrt{\tau_0\mu\dot{\gamma}}, \tag{17.6}$$

while a Herschel–Bulkley fluid is given by

$$\tau = \tau_0 + \mu\dot{\gamma}^n, \tag{17.7}$$

when n is a power-law exponent. Thus, the Herschel–Bulkley fluid is a power-law fluid with a yield stress. Of course, care needs to be taken over applying these formulae when $\dot{\gamma}$ is negative.

With regard to applications, much interest in the flow of Bingham fluids lies in the oil industry. Such fluids include heavy oils, foams, polymer solutions, and viscoelastic surfactants (Sochi and

Blunt 2008). Bingham's original list of yield-stress fluids, quoted in Barnes (1999), includes clay, oil paint, toothpaste, drilling mud, molten chocolate, molten rubbers, and printing inks. To these, Barnes adds ceramic pastes, electro-viscous fluids, thixotropic paints, heavy-duty washing fluids, mayonnaise, yoghurts, purées, liquid pesticides, biomass broths, blood, water–coal mixtures, plastic explosives, and foams. Shenoy (1991) provides the following: certain asphalts and bitumin, fly ash, water suspensions of clay, and sewage sludges. Recent work has considered the modeling of marine sediments (Jeong 2013) and the convection of magma (Maßmeyer 2013). It almost seems that all of life is represented by these examples of yield-stress fluids, notable exceptions being air, water, wine, and beer!

Use of the Bingham law as given by (17.3) is complicated by the fact that the yield surface needs to be found as part of the calculation. For simple flows like Poiseuille flow, Hagen–Poiseuille flow, or the *double glazing* problem (Bayazitoglu et al. 2007), the whole analysis proceeds analytically. But more generally, the yield surface presents very great numerical difficulties. Therefore, authors have modified (termed *regularized*) the law to one which is more amenable to computation. In one dimension, the regularization of Papanastasiou (1987) is given by

$$\tau = \left[\frac{\tau_0}{|\dot{\gamma}|}\left(1 - e^{-m|\dot{\gamma}|}\right) + \mu\right]\dot{\gamma}. \tag{17.8}$$

A schematic of how this law compares with the strict Bingham law is shown in Figure 17.1. From this, we see that at small rates of strain, the effective viscosity is $\mu + m\tau_0$. The approach to the Bingham law then corresponds to $m \to \infty$. The high-viscosity regime inhibits flow but renders the equations much less difficult to solve numerically. A second common approximation is the bilinear law; this too is sketched in Figure 17.1.

Although the computation of Bingham fluid flows is more difficult than for their Newtonian counterparts, some authors have questioned various aspects of the strict Bingham law. Barnes and Walters (1985), for example, have questioned whether there is such a concept as a yield stress. If one views the stress/strain relationship given in Equation 17.3 in terms of an effective viscosity being the

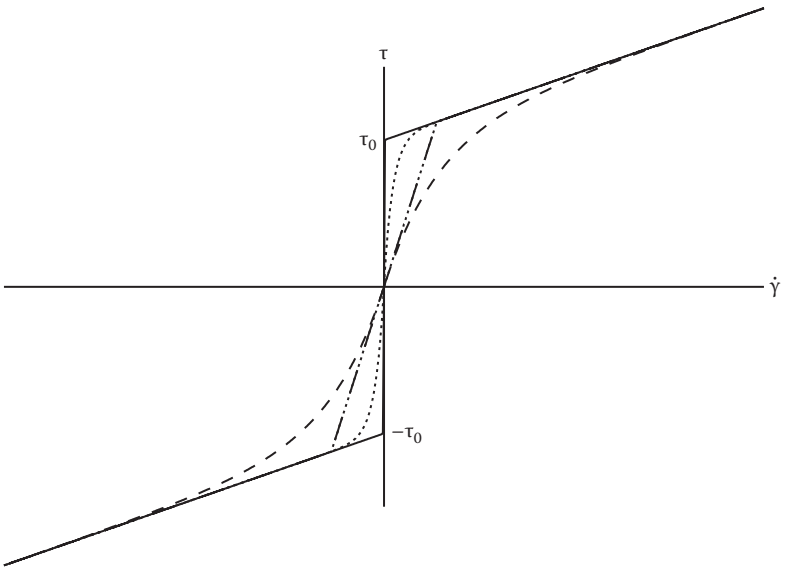

FIGURE 17.1 Displaying the Bingham law (continuous line), Papanastasiou's (1987) regularization with small m (dashes) and large m (dotted), and the bilinear law (dash-dotted).

gradient of the graph shown in Figure 17.1, then at the yield stress, the viscosity suddenly becomes infinite. But Barnes and Walters cite evidence that some fluids possess three different regimes. At high shear rates, the viscosity is constant and therefore Newtonian. At very low shear rates, the fluid is also Newtonian, but the viscosity is very high indeed. Near to what would normally be termed the yield stress, the viscosity changes very rapidly between the two neighboring constant values. In many ways, this is similar to Papanastasiou's regularization.

Cheng (1986) discusses the transient response of fluids with structure. Such fluids may exhibit responses to changing conditions over more than one timescale. There may, for example, be a transient creep response to an imposed shear stress, and this will eventually relax either to no flow or to flow. Thus, the determination of an accurate yield stress depends on when measurements take place, and the accurate computation of flows under changing circumstances may also depend on the relative durations of the creeping response and the externally imposed timescales.

The paper by Liu et al. (2012) discusses the properties of heavy oils. The main message from their work is that the yield stress may, under some circumstances, be temperature dependent. In the case of heavy oils, there exists a temperature, the *converting temperature*, above which the flow is Newtonian. At lower temperatures, there is a yield stress, and its value is proportional to $\ln(T/T_{\text{conv}})$, where T_{conv} is the converting temperature.

Finally, Steffe (1992) sounds a warning note that "an absolute yield stress is an elusive property." By this, it is meant that the yield stress obtained using one experimental technique will often be different from that found by another technique. Such techniques include initiation of movement on an inclined plane, the stress to initiate flow, and backward extrapolation from the flowing regime.

The present author recommends the long paper by Barnes (1999) as a very good first paper to read on the yield stress, and it contains an excellent historical account of the topic.

17.2.2 Flows of Bingham Fluids in Porous Media

In this section, we discuss in some detail the modeling of the flow of a Bingham fluid in a porous medium. The purpose of this subsection is simply to present the various models that have appeared in the literature.

One of the earliest papers to consider such flows is that of Pascal (1981). Citing experimental considerations, a threshold gradient model was chosen, which is the simplest possible model that may be used. Using the notation of this chapter, the one-dimensional form of the threshold model is

$$u = \begin{cases} -\dfrac{K}{\mu}\left[1 - \dfrac{G}{|p_x|}\right] p_x & \text{when } |p_x| > G, \\ 0 & \text{otherwise,} \end{cases} \tag{17.9}$$

where we use G to denote the threshold gradient. A more complicated relationship is given by the Buckingham–Reiner (or BR) model. In the present context, we may write this as

$$u = \begin{cases} -\dfrac{K}{u}\left[1 - \dfrac{4}{3}\left(\dfrac{G}{|p_x|}\right) + \dfrac{1}{3}\left(\dfrac{G}{|p_x|}\right)^4\right] p_x & \text{when } |p_x| > G, \\ 0 & \text{otherwise,} \end{cases} \tag{17.10}$$

although a very wide range of notations may be found in the literature. This model is derived by assuming that the porous medium consists of a bundle of identical circular cross-sectioned tubes for which an exact solution of the polar coordinate form of Equations 17.2 and 17.3 may be found. Thus, we have Hagen–Poiseuille flow. The mean flow is then averaged and finally expressed in a form where K denotes the overall permeability of the same configuration when saturated with a Newtonian fluid.

A similar procedure will be used in Section 17.3 for plane channels. This model has been adopted by many authors including Balhoff and Thompson (2004) and Mendes et al. (2002).

The corresponding form for plane channels in which Poiseuille flow exists is what we shall term the plane Buckingham–Reiner (or BR2D) model; it is,

$$u = \begin{cases} -\dfrac{K}{\mu}\left[1 - \dfrac{3}{2}\left(\dfrac{G}{|p_x|}\right) + \dfrac{1}{2}\left(\dfrac{G}{|p_x|}\right)^3\right] p_x & \text{when } |p_x| > G, \\ 0 & \text{otherwise.} \end{cases} \tag{17.11}$$

Both the standard and the plane Buckingham–Reiner models are shown in Figure 17.2, together with the threshold model for comparison. It may be seen that there is a gradual rise in the velocity as the driving pressure gradient passes the threshold value. If one were to allow the pressure gradient to be just above the threshold value, that is, $-p_x = G(1 + \epsilon)$, where ϵ is small and positive, then the standard and plane Buckingham–Reiner models yield

$$u \simeq -\frac{K}{\mu}\left[2\epsilon^2 + \cdots\right] p_x, \quad \text{and} \quad u \simeq -\frac{K}{\mu}\left[\frac{3}{2}\epsilon^2 + \cdots\right] p_x, \tag{17.12}$$

respectively, and therefore the linear rise of the threshold model immediately post yield is replaced by a quadratic rise. One may also consider the reciprocal of the slopes of the curves given in Figure 17.2 as being the effective viscosities for the three models.

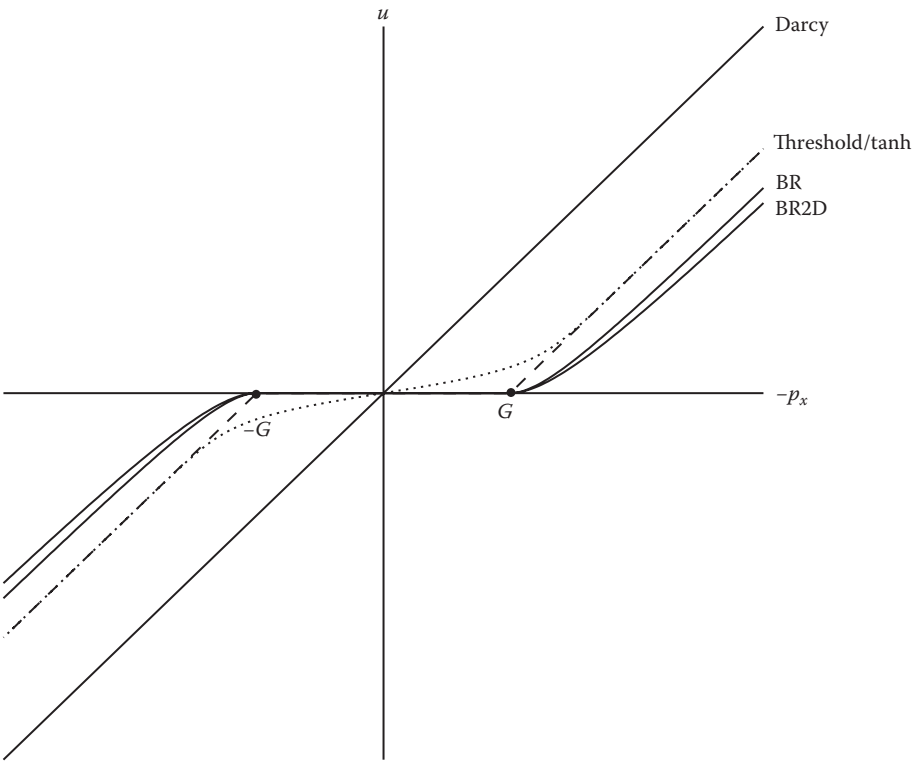

FIGURE 17.2 Displaying Darcy's law, the threshold law (dashed line), the tanh law (dotted line), and the two Buckingham–Reiner laws.

The final model takes the form of a regularization similar in intent to that of Papanastasiou (1987) mentioned earlier. We will name it the tanh model, and it takes the form

$$\left[1 + G\frac{K}{\mu}\frac{\tanh(cu)}{u}\right]u = -\frac{K}{\mu}p_x. \tag{17.13}$$

This fourth model is shown in Figure 17.2 as the dotted line, and the presence of the tanh function causes the effective viscosity to become large under small pressure gradients. More precisely, the effective viscosity rises from its large pressure gradient value of μ to the value, $\mu + GKc$, as the pressure gradient decreases toward zero. This model holds very distinct advantages over the other three when numerical computations are required. The threshold model is difficult to implement because of the need to determine the yield surface. The two BR models have the same difficulty, but u is also a nonlinear function of the pressure gradient in the yielded regime. Thus, if one wished to solve a two-dimensional convection problem using the streamfunction, then (1) one would need to apply the appropriate Cardan solution for a cubic (for the BR2D model) or the appropriate Ferrari solution for a quartic (for the BR model) in order to find p_x in terms of u, and (2) the yield surface still needs to be found. On the other hand, the tanh model suffers from none of these defects. As we will see later, the equation for the streamfunction in the tanh model becomes nonlinear, but the numerical difficulties associated with that aspect are relatively small.

We note, finally, that all four models have to take suitably modified forms when considering flows in two and three dimensions. These will be introduced as necessary later.

17.3 ISOTHERMAL FLOWS OF A BINGHAM FLUID IN A POROUS MEDIUM

We will consider plane Poiseuille flow in channels. From this, we will derive the BR2D model mentioned earlier, extend it first to cases where the bundle of channels consists of channels of different width, and second to a continuous distribution of channels. Finally, a square network of channels of identical widths will be considered, and this is used to demonstrate a natural anisotropy that arises because of the presence of the yield stress but which is absent when the fluid is Newtonian. It is important to note that much of this section is taken from Nash (2013).

17.3.1 Plane Buckingham–Reiner Model

We consider the motion of a Bingham fluid in a uniform channel of width h under the action of the pressure gradient, $-p_x$. For mathematical convenience, the channel has boundaries at $y = \pm h/2$, and for presentational convenience, we will set $G = -p_x > 0$ to be the pressure gradient. We may solve Equation 17.2 easily and apply the appropriate symmetry to show that

$$\tau = -Gy. \tag{17.14}$$

Therefore, it is clear that $-Gh/2 \le \tau \le Gh/2$ in the channel. If $Gh/2 < \tau_0$ is satisfied, then there will be no flow. If there is flow, then the yield surfaces will lie where $Gy = \pm\tau_0$. Let this be at $y = \pm\epsilon h/2$, where ϵ denotes the fraction of the channel that is unyielded. Thus, we find that

$$\epsilon = \frac{2\tau_0}{Gh}. \tag{17.15}$$

The solution is shown in Figure 17.3 together with the solutions in the various yielded and unyielded portions of the channel.

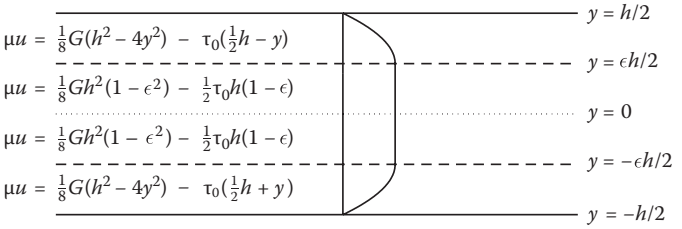

FIGURE 17.3 Displaying the velocity profile for the Poiseuille flow of a Bingham fluid in a channel.

The total volumetric flux, Q, is given by

$$\mu Q = \int_{-h/2}^{h/2} u dy = \begin{cases} \dfrac{Gh^3}{12}\left[1 - \dfrac{3\epsilon}{2} + \dfrac{\epsilon^3}{2}\right] & \text{when } G > \dfrac{2\tau_0}{h}, \\ 0 & \text{when } 0 \le G \le \dfrac{2\tau_0}{h}, \end{cases} \tag{17.16}$$

and thus

$$G = \frac{2\tau_0}{h} \tag{17.17}$$

is the yield pressure gradient. Equation 17.16 may now be written in terms of a scaled pressure gradient, σ, where

$$\sigma = \frac{1}{\epsilon} = \frac{Gh}{2\tau_0}. \tag{17.18}$$

Hence we have,

$$\mu Q = \frac{Gh^3}{12} f(\sigma), \tag{17.19}$$

where

$$f(\sigma) = \begin{cases} 1 - \dfrac{3}{2|\sigma|} + \dfrac{1}{2|\sigma|^3} & \text{when } |\sigma| \ge 1, \\ 0 & \text{when } |\sigma| \le 1. \end{cases} \tag{17.20}$$

Equation 17.19 is the BR2D law, which was introduced earlier, though now in nondimensional form using the function, $f(\sigma)$. It is also in a form in which Equation 17.19 applies for either possible sign for G.

If we consider a porous medium to consist of a periodic array of channels of width h and with period H, then the Darcy velocity of the Bingham fluid through that medium is

$$u_{DB} = \frac{1}{H}\int_{-H/2}^{H/2} u dy = \frac{\phi G h^2}{12\mu} h^2 f(\sigma), \tag{17.21}$$

where $\phi = h/H$ is the porosity. The corresponding Darcy velocity of a Newtonian fluid is $u_D = \phi G h^2/12\mu$, and therefore $f(\sigma)$ is the ratio of the two velocities.

17.3.2 Modifications for Multiple Channels

If one now considers that the periodic bundle of channels contains one channel of width h and a second one of width γh per period where $\gamma < 1$, then we may simply add the appropriate forms of Equation 17.19:

$$\mu Q = \begin{cases} 0 & \sigma\gamma < \sigma < 1, \\ \dfrac{Gh^3}{12} f(\sigma) & \sigma\gamma < 1 < \sigma, \\ \dfrac{Gh^3}{12}\left[f(\sigma) + \gamma^3 f(\sigma\gamma)\right] & 1 < \gamma\sigma < \sigma. \end{cases} \tag{17.22}$$

The porosity is now $\phi = h(1 + \gamma)/H$, and therefore the Darcy–Bingham velocity is

$$u_{\mathrm{DB}} = \begin{cases} 0 & \sigma\gamma < \sigma < 1, \\ \dfrac{\phi Gh^2}{12\mu} \dfrac{f(\sigma)}{1+\gamma} & \sigma\gamma < 1 < \sigma, \\ \dfrac{\phi Gh^2}{12\mu} \dfrac{f(\sigma) + \gamma^3 f(\sigma\gamma)}{1+\gamma} & 1 < \gamma\sigma < \sigma. \end{cases} \tag{17.23}$$

In these formulae, three different forms of expression have been used purely to differentiate between the three different regimes: (1) no flow, (2) flow in the wider channel, and (3) flow in both channels. Given the definition of $f(\sigma)$ in Equation 17.20, noting specifically that it takes zero values when $\sigma < 1$, then we may formally use the third expression in Equation 17.23 in all cases.

These expressions may be generalized further by taking N channels per period, where the channel widths are taken to be $\gamma_i h$, $i = 1, \ldots, N$, and where

$$1 = \gamma_1 \geq \gamma_2 \geq \gamma_3 \geq \cdots \geq \gamma_N. \tag{17.24}$$

This definition allows for multiple instances of any chosen width. For this system, the Darcy velocity is now

$$u_{\mathrm{DB}} = \frac{\phi Gh^2}{12\mu}\left[\frac{\sum_{i=1}^{N} \gamma_i^3 f(\sigma\gamma_i)}{\sum_{i=1}^{N} \gamma_i}\right]. \tag{17.25}$$

Some representative cases are shown in Figure 17.4 in the form of a scaled Darcy velocity, that is, the figure shows the velocity relative to that of a Newtonian fluid.

The single channel is the uppermost curve, and this represents the variation of $f(\sigma)$. At first, it may seem surprising that the addition of narrower channels appears to reduce the Darcy velocity for a given σ, but this is due to the redefinition of the porosity, ϕ. We may say, therefore, that for a given porosity, ψ, the *scaled* Darcy velocity (which is what is shown in Figure 17.4) will decrease whenever extra channels are introduced because the velocity flux of the Bingham fluid then decreases relative to that of the corresponding Newtonian fluid.

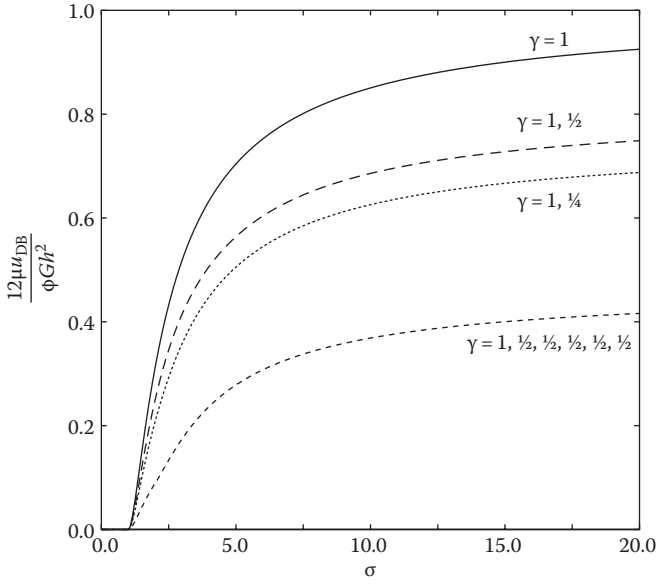

FIGURE 17.4 Displaying the Darcy velocity for different sets of channel bundles.

17.3.3 Distributions of Channels

In practice, a porous medium is most likely to be formed from channels that have randomly distributed widths. If this distribution is taken to be uniform, for example, then a uniform distribution of channels in the range, $a \leq \gamma \leq 1$, yields the following:

$$u_{DB} = \frac{\phi G h^2}{12\mu}\left[\frac{\int_a^1 \gamma^3 f(\sigma\gamma)\mathcal{H}(\sigma\gamma - 1)d\gamma}{\int_a^1 \gamma d\gamma}\right], \tag{17.26}$$

where $\mathcal{H}$ is the Heaviside or unit step function; this has been included to ensure that due care is taken with the integral and simply represents the fact that $f(\sigma\gamma) = 0$ when $\sigma\gamma < 1$. Hence,

$$\frac{12\mu u_{DB}}{\phi G h^2} = \begin{cases} 0 & \sigma < 1, \\ \dfrac{(\sigma-1)^3(\sigma+1)}{2\sigma^4(1-a^2)} & 1 < \sigma < \dfrac{1}{a}, \\ \dfrac{1+a^2}{2} - \dfrac{1+a+a^2}{(1+a)\sigma} + \dfrac{1}{\sigma^3(1+a)} & \dfrac{1}{a} < \sigma. \end{cases} \tag{17.27}$$

The behavior of this function for three different values of a may be found in Figure 17.5. We note that when σ is just above 1, then the Darcy velocity rises initially as a cubic, rather than as a quadratic as happens for a single channel, given the factor $(\sigma - 1)^3$ in the second line of Equation 17.27.

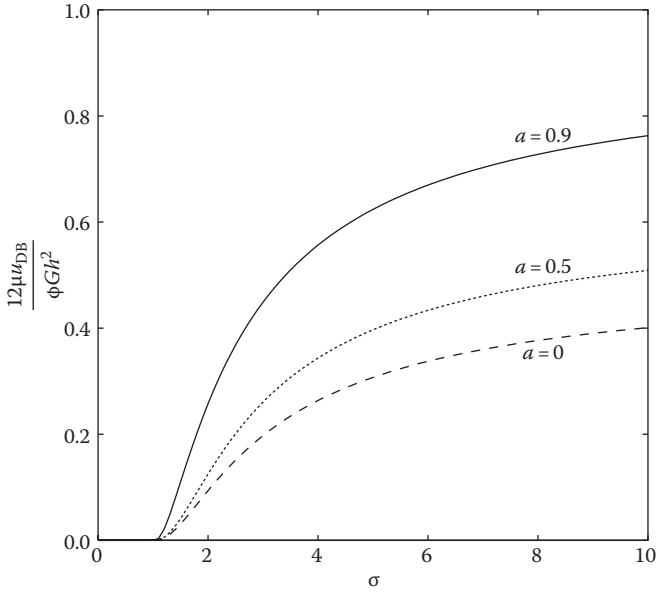

FIGURE 17.5 Displaying the Darcy velocity for uniformly distributed channels.

It is also interesting to note that we are able to recover the BR2D formula given by Equation 17.21 from Equation 17.27 by taking the limit $a \to 1$. In this limit, the intermediate regime, namely, $1 < \sigma < 1/a$, disappears, while the $\sigma > 1/a$ regime reproduces the BR2D formula.

17.3.4 Flow through a Network: Yield-Stress-Induced Anisotropy

Although we have not exhausted the possibilities for one-dimensional flow—one may also consider different types of discrete and continuous distributions of both channels and tubes—we turn now to a simple square network of uniform channels. These channels are aligned in the x- and y-directions, and are of width h again where each channel is separated from its nearest parallel neighbor by a distance, H. Thus, the analysis of Section 17.3.1 applies. We also note the assumption that $h \ll H$ so that the interactions at intersections may be neglected at leading order.

A sketch of the square network of channels is given in Figure 17.6. A pressure gradient of magnitude G is applied to this network at an angle, θ_G, to the horizontal (x) direction. This pressure gradient may be resolved into its two horizontal and vertical components, and the analysis of Section 17.3.1 applied to each direction separately by means of the appropriate modifications of Equation 17.21. Therefore, we obtain

$$\frac{12\mu u_{DB}}{\phi G h^2} = f(\sigma_x)\cos\theta_G, \qquad \sigma_x = \frac{Gh\cos\theta_G}{2\tau_0}, \tag{17.28}$$

$$\frac{12\mu v_{DB}}{\phi G h^2} = f(\sigma_y)\sin\theta_G, \qquad \sigma_y = \frac{Gh\sin\theta_G}{2\tau_0}. \tag{17.29}$$

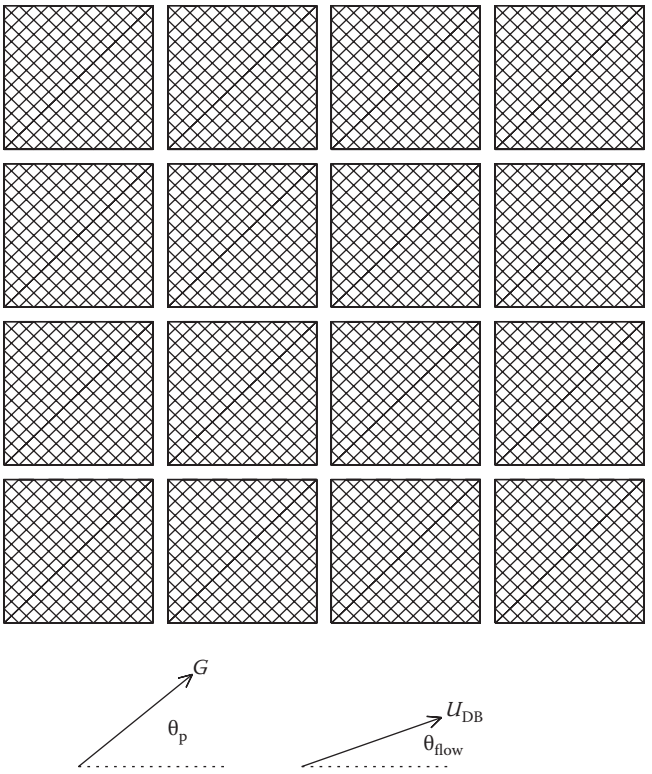

FIGURE 17.6 Showing a square network of channels.

From these expressions, we may determine the total velocity which has been induced and its direction:

$$\frac{12\mu\,|\,\underline{u}\,|_{\mathrm{DB}}}{\phi G h^2} = \sqrt{\left[f(\sigma_x)\cos\theta_G\right]^2 + \left[f(\sigma_y)\sin\theta_G\right]^2} \quad \text{and} \quad \tan\theta_{\mathrm{flow}} = \frac{f(\sigma_y)\sin\theta_G}{f(\sigma_x)\cos\theta_G}. \tag{17.30}$$

The variation of the magnitude of the induced flow and its direction with both G and the orientation of the applied pressure gradient, θ_G, are shown in Figure 17.7. Here, we see that the magnitude of the velocity varies with θ_G, and when $\sigma < \sqrt{2}$, there are directions centered on 45° where the pressure gradient is insufficient to drive a flow. The maximum velocity for a given G is always attained when the pressure gradient is in the direction of the channels, while the minimum always corresponds to it being at an orientation of 45°.

We also see that when σ takes relatively small values, the flow will often be either in the horizontal or in the vertical direction. This is because the component of the pressure gradient in the direction orthogonal to the flow is insufficient to cause yield. Thus, we see a rapid change in the direction of the induced flow near to $\theta_G = 45°$ as θ_G varies from 0° to 90°. But as G increases, we find that variations in velocity tend to vanish and $\theta_f \to \theta_G$. Thus, the large-G limit, the Newtonian limit, yields an isotropic system where the underlying grid of channels is not evident in the response of the fluid to the pressure gradient. Therefore, for a Bingham fluid, we have a strong anisotropy in the response to an applied pressure gradient, one that is caused by the presence of the yield stress, and which is entirely absent when the fluid is Newtonian.

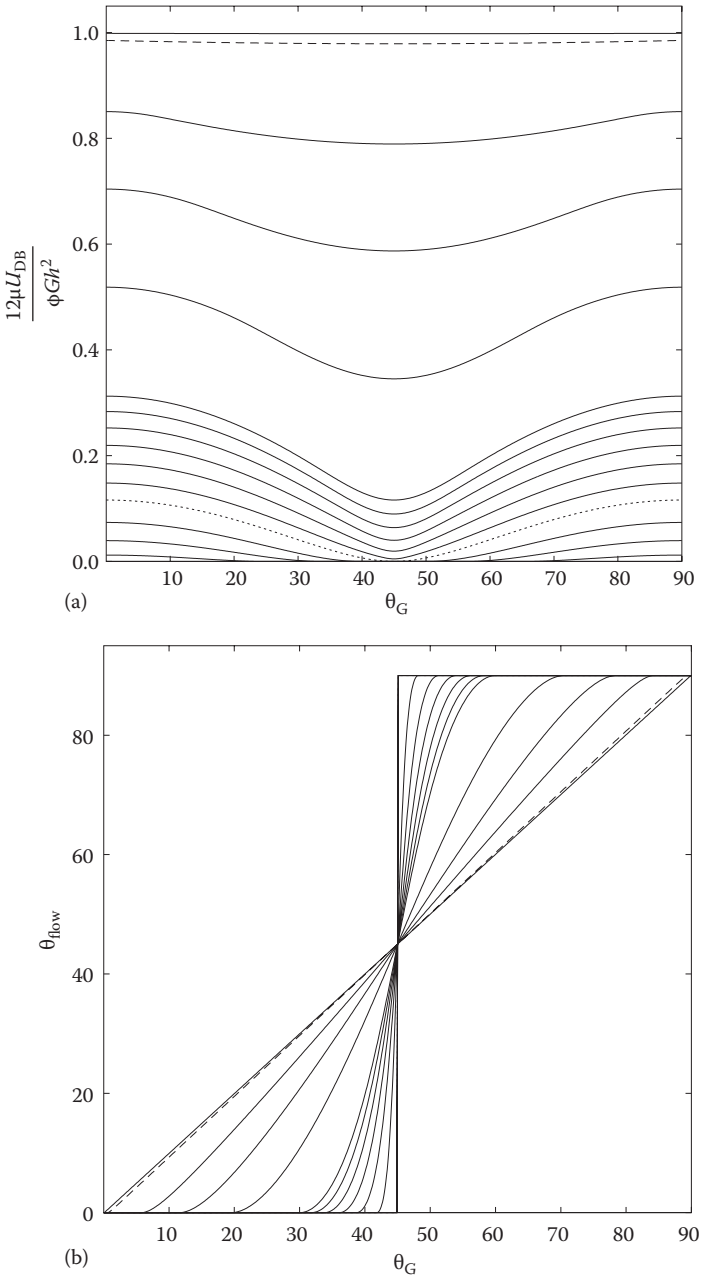

FIGURE 17.7 Displaying (a) the Darcy velocity and (b) the direction of flow for $\sigma = 1.1, 1.2, 1.3, \sqrt{2}$ (dotted), 1.5, 1.6, 1.7, 1.8, 1.9, 2, 3, 5, 10, 100 (dashed), and 1000. Angles are in degrees.

17.4 NETWORK MODELING OF THE CONVECTION OF A BINGHAM FLUID IN A POROUS MEDIUM

We may apply the same network modeling ideas to problems involving convection. Thus far, we have been interested in isothermal flows, and therefore we need to adapt some of our earlier analyses to allow for buoyancy as a body force.

17.4.1 Convection in a Sidewall-Heated Vertical Layer Formed of Channels

We will consider a porous medium that consists of $N + 1$ identical narrow vertical channels through which a Bingham fluid may flow. These channels are separated by N identical solid regions. The channels have width h, and the overall vertical layer is of width H where $h \gg H$. The layer is depicted in Figure 17.8, and we see that there is a temperature drop of magnitude ΔT across the layer. We have no need to consider the effect of having different conductivities of the fluid and the solid because the buoyancy force will depend on the magnitude of the departure of the fluid temperature from the reference value, rather than the temperature drop across the fluid channel. This scenario will change only when the fluid-to-solid thermal conductivity ratio is of the same order of magnitude as h/H.

We intend to work from this point forward in nondimensional terms, and therefore our earlier work needs to be reformulated. For channels of dimensional width, h, under the action of a pressure gradient, $-G$, the volumetric flux along one channel may be written in the form $Q = (h^3/12\mu)Gf(\sigma)$, where $\sigma = Gh/2\tau_0$. This form allows for pressure gradients of either sign. After averaging in the usual way, the overall (Newtonian) permeability of the layer shown in Figure 17.8 is, therefore, $K = (N + 1)h^3/12H$ or $\phi h^2/12$, where ϕ is the porosity. Therefore, we may write

$$Q = \frac{K}{(N+1)\mu} Gf(\sigma) \tag{17.31}$$

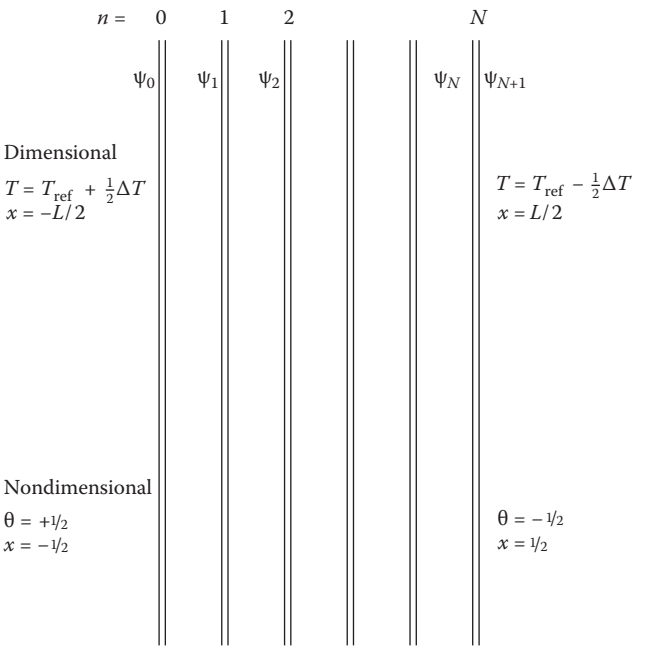

FIGURE 17.8 Displaying a vertical layer with thin vertical channels subject to sidewall heating and cooling. Both the dimensional and nondimensional boundary conditions are shown.

for the volumetric flux in *one* channel. Previously, we had $G = -p_x$, which denoted a pressure gradient in the x-direction. Now we replace the pressure gradient by the buoyancy force, and therefore we set $G = \rho g\beta(T - T_{\text{ref}})$, where ρ is the density of the fluid at the reference temperature, T_{ref} (which is at the center of the layer), g is the gravity, and β is the volumetric expansion coefficient. Additionally, the Boussinesq approximation has been assumed. Therefore, Equation 17.31 becomes

$$Q = \frac{K}{(N+1)\mu}\rho g\beta(T - T_{\text{ref}})f(\sigma), \tag{17.32}$$

where

$$\sigma = \rho g\beta(T - T_{\text{ref}})\frac{h}{2\tau_0}. \tag{17.33}$$

Now we will rescale according to

$$Q_{\text{dim}} = \frac{\alpha}{L(N+1)}Q_{\text{nondim}}, \quad T = T_{\text{ref}} + \Delta T\theta. \tag{17.34}$$

This has the effect of changing Equations 17.32 and 17.33 to the nondimensional forms

$$Q = \text{Ra}\,\theta f(\sigma) \quad \text{where } \sigma = \text{Ra}\,\theta/\text{Rb}, \tag{17.35}$$

where the Darcy–Rayleigh number and a dimensionless yield stress are defined as

$$\text{Ra} = \frac{\rho g\beta\Delta TKL}{\mu\alpha} \quad \text{and} \quad \text{Rb} = \frac{2\tau_0}{h}\frac{KL}{\mu\alpha}. \tag{17.36}$$

In the rest of this chapter, these two numbers will be referred to as the Rayleigh and Rees–Bingham numbers, respectively, although we need to note that a Bingham number defined by $\text{Bn} = \tau_0 L/\mu V$, where V is a velocity, is already well known in other contexts and represents the ratio of yield stresses (τ_0) and viscous stresses ($\mu V/L$). We also note that the earlier expression for the Rees–Bingham number contains the group, $2\tau_0/h$, which is the yield pressure gradient (or body force) for flow in a one-dimensional system of channels of width, h, as described in the previous section. More generally, therefore, we may write the Rees–Bingham number as

$$\text{Rb} = \frac{GKL}{\mu\alpha}, \tag{17.37}$$

where $|G|$ is the magnitude of the pressure gradient above which the fluid flows.

Finally, we note that the value, Q, may also be interpreted as the difference between the nondimensional streamfunction values on the two sides of the narrow channels, and Figure 17.8 denotes how we label the different values of the streamfunction. The nondimensional boundary conditions are as shown in Figure 17.8, and therefore the temperature field is simply, $\theta = -x$. From this, we see that the maximum buoyancy force corresponds to the two outer channels (i.e., numbers 0 and N) for which $x = \pm 1/2$. Therefore, as the Rayleigh number increases, flow will arise first in those channels. Using Equation 17.35 and setting $\sigma = \pm 1$, we find that the condition for this happening is that

$$\text{Ra} > 2\text{Rb}. \tag{17.38}$$

The neighboring channels, $n = 1$ and $n = N - 1$, correspond to $x = \pm(N - 2)/2N$, and therefore fluid begins to flow in these channels when

$$\mathrm{Ra} > 2\mathrm{Rb}\frac{N}{N-2}. \tag{17.39}$$

In a similar fashion, the next two channels, $n = 2$ and $n = N - 2$, which are located at $x = \pm(N - 4)/2N$, begin to admit flow when

$$\mathrm{Ra} > 2\mathrm{Rb}\frac{N}{N-4}, \tag{17.40}$$

with the obvious extension to further channels.

We see that convective *onset* happens at discrete values of Ra with increasing numbers of channels admitting flow as the Rayleigh number increases.

17.4.2 Convection in a Sidewall-Heated Square Cavity

We now consider convection in a square cavity of the type depicted in Figure 17.6, but the detailed analysis begins with one block as shown in Figure 17.9.

Within the horizontal channels, we have $\tau_z = -p_x$, and in the vertical channels, $\tau_x = -p_z + \mathrm{Ra}\,\theta$. The subscript notation on the G–values in Figure 17.9 denotes the compass directions. Convection is assumed to be weak in the sense that it is not strong enough to modify the temperature field from $\theta = -x$. The streamfunction is set to be zero on the outer boundary.

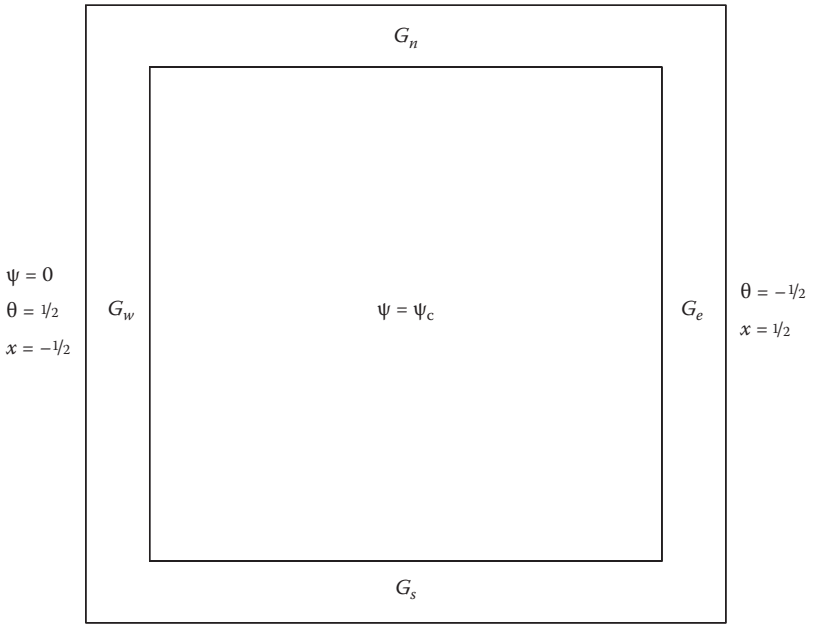

FIGURE 17.9 Displaying the single-block case of a network of channels showing the streamfunction values and the notation for the body force terms.

The following network analysis follows the method outlined in Jamalud-Din et al. (2010). On applying the general theory derived earlier and which is represented by Equation 17.35, we obtain the following equations for each of the four channels surrounding the central block:

$$\begin{aligned}
&\text{West:} && \psi_c = G_w f(\sigma_w) && G_w = -\left.\frac{\partial p}{\partial z}\right|_w + \frac{1}{2}\mathrm{Ra}, && \sigma_w = \frac{G_w}{\mathrm{Rb}},\\
&\text{East:} && -\psi_c = G_e f(\sigma_e) && G_e = -\left.\frac{\partial p}{\partial z}\right|_e - \frac{1}{2}\mathrm{Ra}, && \sigma_e = \frac{G_e}{\mathrm{Rb}},\\
&\text{South:} && -\psi_c = G_s f(\sigma_s) && G_s = -\left.\frac{\partial p}{\partial x}\right|_s, && \sigma_s = \frac{G_s}{\mathrm{Rb}},\\
&\text{North:} && \psi_c = G_n f(\sigma_n) && G_n = -\left.\frac{\partial p}{\partial x}\right|_n, && \sigma_n = \frac{G_n}{\mathrm{Rb}}.
\end{aligned} \tag{17.41}$$

To these equations, we must add the condition that the pressure difference between the bottom left corner and the top right corner is independent of the direction of travel:

$$\left.\frac{\partial p}{\partial z}\right|_w + \left.\frac{\partial p}{\partial x}\right|_n = \left.\frac{\partial p}{\partial z}\right|_e + \left.\frac{\partial p}{\partial x}\right|_s. \tag{17.42}$$

The solution of this system of five equations is

$$\sigma_w = \sigma_n = -\sigma_e = -\sigma_s = \frac{\mathrm{Ra}}{4\mathrm{Rb}}, \quad \psi_c = \frac{\mathrm{Ra}}{4} f(\sigma) \quad \text{where } \sigma = \frac{\mathrm{Ra}}{4\mathrm{Rb}}. \tag{17.43}$$

Given that flow takes place in the channels only when $\sigma > 1$, we conclude that convection begins when $\mathrm{Ra} = 4\mathrm{Rb}$. This is double the value that was found for the vertical layer in Section 17.4.1. This may be justified by appealing to the fact that, for a unit vertical distance, the buoyancy forces need to move the fluid through twice the distance in the cavity than they do in the vertical layer.

We may now extend this analysis to larger systems of blocks within the square cavity. A definition sketch of a 3×3 system is shown in Figure 17.10, where, for convenience, a new notation for the body force in the horizontal (H_{ij}) and vertical (V_{ij}) channels is introduced.

Here, $H_{ij} = -p_x$ and $V_{ij} = -p_z + \mathrm{Ra}\, x_i$ denote the horizontal and vertical body forces, respectively, while $x_1 = -1/2$, $x_2 = -1/6$, $x_3 = -1/6$, and $x_4 = 1/2$. On applying the same method as for the single-block case, we obtain the following set of 33 equations for 33 unknowns:

$$\begin{aligned}
\psi_{11} &= V_{11} f(V_{11}/\mathrm{Rb}) & \psi_{11} &= -H_{11} f(H_{11}/\mathrm{Rb}) & V_{11} + H_{12} &= H_{11} + V_{21} + \mathrm{Ra}/3\\
\psi_{12} &= V_{12} f(V_{12}/\mathrm{Rb}) & \psi_{21} &= -H_{21} f(H_{21}/\mathrm{Rb}) & V_{21} + H_{22} &= H_{21} + V_{31} + \mathrm{Ra}/3\\
\psi_{13} &= V_{13} f(V_{13}/\mathrm{Rb}) & \psi_{31} &= -H_{31} f(H_{31}/\mathrm{Rb}) & V_{31} + H_{32} &= H_{31} + V_{41} + \mathrm{Ra}/3\\
\psi_{21} - \psi_{11} &= V_{21} f(V_{21}/\mathrm{Rb}) & \psi_{12} - \psi_{11} &= -H_{12} f(H_{12}/\mathrm{Rb}) & V_{12} + H_{13} &= H_{12} + V_{22} + \mathrm{Ra}/3\\
\psi_{22} - \psi_{21} &= V_{22} f(V_{22}/\mathrm{Rb}) & \psi_{22} - \psi_{21} &= -H_{22} f(H_{22}/\mathrm{Rb}) & V_{22} + H_{23} &= H_{22} + V_{32} + \mathrm{Ra}/3\\
\psi_{23} - \psi_{13} &= V_{23} f(V_{23}/\mathrm{Rb}) & \psi_{32} - \psi_{31} &= -H_{32} f(H_{32}/\mathrm{Rb}) & V_{32} + H_{33} &= H_{32} + V_{42} + \mathrm{Ra}/3\\
\psi_{31} - \psi_{21} &= V_{31} f(V_{31}/\mathrm{Rb}) & \psi_{13} - \psi_{12} &= -H_{13} f(H_{13}/\mathrm{Rb}) & V_{13} + H_{14} &= H_{13} + V_{23} + \mathrm{Ra}/3\\
\psi_{32} - \psi_{22} &= V_{32} f(V_{32}/\mathrm{Rb}) & \psi_{23} - \psi_{22} &= -H_{23} f(H_{23}/\mathrm{Rb}) & V_{23} + H_{24} &= H_{23} + V_{33} + \mathrm{Ra}/3\\
\psi_{33} - \psi_{23} &= V_{23} f(V_{23}/\mathrm{Rb}) & \psi_{33} - \psi_{32} &= -H_{33} f(H_{33}/\mathrm{Rb}) & V_{33} + H_{34} &= H_{33} + V_{43} + \mathrm{Ra}/3\\
-\psi_{31} &= V_{41} f(V_{41}/\mathrm{Rb}) & -\psi_{13} &= -H_{14} f(H_{14}/\mathrm{Rb}) & &\\
-\psi_{32} &= V_{42} f(V_{42}/\mathrm{Rb}) & -\psi_{23} &= -H_{24} f(H_{24}/\mathrm{Rb}) & &\\
-\psi_{33} &= V_{43} f(V_{43}/\mathrm{Rb}) & -\psi_{33} &= -H_{34} f(H_{34}/\mathrm{Rb}) & &
\end{aligned} \tag{17.44}$$

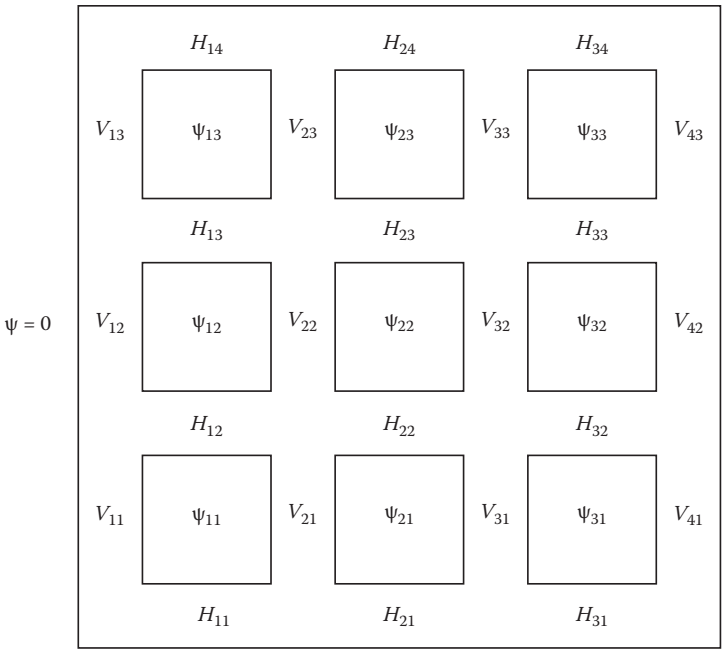

FIGURE 17.10 Displaying the 3 × 3 system of identical blocks within a square cavity.

These equations were solved using a general-purpose user-written Newton–Raphson program using numerical differentiation to obtain the Jacobian matrix. However, the Jacobian matrix is singular whenever the fluid is unyielded in any channel, and therefore, we have adopted the following regularization-like modification to the definition of $f(\sigma)$:

$$f(\sigma) = \begin{cases} \left(1 - \dfrac{3}{2|\sigma|} + \dfrac{1}{|\sigma|^3}\right) + \epsilon|\sigma| & |\sigma| > 1, \\ \epsilon|\sigma| & 0 < |\sigma| < 1, \end{cases} \tag{17.45}$$

where we took $\epsilon = 10^{-5}$, which is small enough to affect the resulting solutions minimally, but large enough to allow solutions to be obtained robustly.

Figure 17.11 shows how the streamfunction values vary with the Rayleigh number for this 3 × 3 system of blocks and for a 9 × 9 system. The abscissae in this figure are both Ra/4Rb because curves for different values of Rb collapse down to a unique curve when this is done. In fact, one may rescale the variables in Equation 17.44 so that the dependence on Ra/Rb becomes explicit.

As with the vertical channel, we see successive bifurcations within these two cases as increasing numbers of channels begin to flow as Ra increases. A detailed examination of the numerical solutions indicate that the first bifurcation to flow arises when Ra = 4Rb, as for the single-block case. This indicates that only the outermost circuit flows when Ra is slightly above this value. Successive bifurcations, which are indicated by black disks in the figure, then correspond to new square circuits being released to flow.

For the 3 × 3 system, the bifurcations arise when Ra/4Rb = 1 and 3, while for the 9 × 9 system, they arise at Ra/4Rb = 1, 9/7, 9/5, 3, and 9. Indeed, for odd values of N, successive bifurcations happen when Ra/4Rb = N/j where $j = N, N-2, N-4, \ldots, 1$. For even values, the same sequence happens

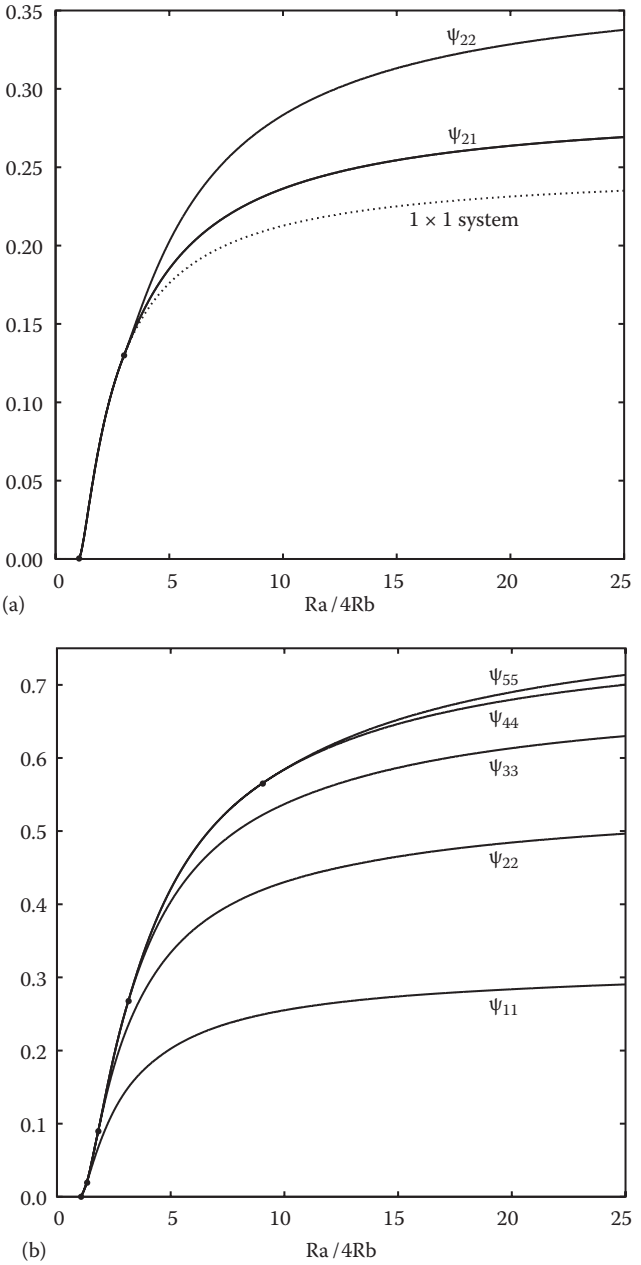

FIGURE 17.11 The variation of ψ with Rayleigh number for a (a) 3 × 3 and a (b) 9 × 9 system of blocks. The dotted line indicates the variation of ψ for the single-block system.

but ends with $j = 2$, in which case the central 2 × 2 system has no flow between its blocks, and these four act as a single block of double the linear dimension.

These observations may be explained by appealing to the temperature drop across each of these successively smaller square circuits; the value of Ra/4Rb is then the reciprocal of the width of that circuit compared with that of the square cavity.

No doubt a different network morphology will yield quite different results from those presented here, and it is intended to pursue this aspect in the immediate future.

17.5 CONVECTION OF A BINGHAM FLUID IN A SIDEWALL-HEATED CAVITY

This section is devoted to analyzing convection, which is caused by heating a sidewall in a vertical channel or cavity. The major difference between this section and Section 17.4 is that we will now be employing macroscopic laws for the momentum equations, ones that are motivated by our previous results. Thus, our aim is to consider strongly nonlinear convection and to determine how the different types of Darcy–Bingham law that arise will affect the flow pattern and the strength of convection.

We will consider two different systems briefly. The first is the so-called double glazing problem where the porous medium is confined between two vertical impermeable vertical surfaces that are held at temperatures that are steady and uniform but that are different. The second is a square cavity with the same sidewall heating and cooling, but where the upper and lower surfaces are insulating. This is a classic test case for numerical computation for porous cavities, but especially for clear fluids with high Rayleigh numbers. This second system is divided into three cases that are distinguished by the type of Darcy–Bingham law which is used. In the first case, we consider an isotropic threshold gradient law as modified/regularized for computational reasons by a tanh profile. The second is an anisotropic form that is equivalent to the square grid pattern used in the network modeling of Section 17.4.1. Here there are preferential flow directions for the Bingham fluid, and these are in the x- and z-directions. Then, the third case allows for these preferential directions to be rotated by an angle, α.

17.5.1 The Double Glazing Problem

The configuration we study is identical to that shown in Figure 17.8 except that we now adopt a macroscopic law to replace the channels that were considered in Section 17.4.1.

The channel is presumed to have infinite height, and therefore the flow, whenever it arises, will be in the vertical direction, z, and will be a function of x only. The nondimensional macroscopic equation for the vertical velocity is

$$w = f(\sigma_z)\left[-\frac{\partial p}{\partial z} + \mathrm{Ra}\theta\right], \tag{17.46}$$

where

$$\sigma_z = \frac{1}{\mathrm{Rb}}\left[-\frac{\partial p}{\partial z} + \mathrm{Ra}\theta\right], \quad \text{and} \quad \theta = -x. \tag{17.47}$$

This one-dimensional equation is the natural upscaled version of Equation 17.35, which describes Darcy–Bingham flow based on the BR2D model for microscopic flows in channels.

We now set $\partial p/\partial z = 0$ in order to maintain a zero overall fluid flux up the layer, and therefore we obtain $w = -\mathrm{Ra}\, x\, f(-\mathrm{Ra}\, x/\mathrm{Rb})$. This velocity profile may therefore be written in the form

$$w = \begin{cases} -\mathrm{Ra}\, x\left[1 - \dfrac{3\mathrm{Rb}}{2\mathrm{Ra}\,|x|} + \dfrac{\mathrm{Rb}^3}{\mathrm{Ra}^3\,|x|^3}\right] & \text{when} \quad \left|\dfrac{\mathrm{Ra}\, x}{\mathrm{Rb}}\right| > 1. \\ 0 & \text{when} \quad \left|\dfrac{\mathrm{Ra}\, x}{\mathrm{Rb}}\right| < 1. \end{cases} \tag{17.48}$$

Clearly, convection begins when $\mathrm{Ra} = 2\mathrm{Rb}$, as with the earlier discretely layered vertical channel, and immediately post-onset convection is confined to those regions near the external walls.

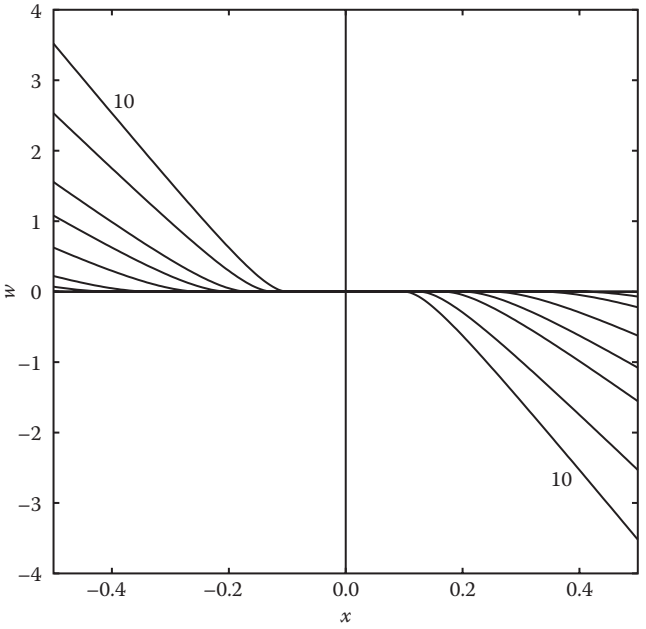

FIGURE 17.12 Velocity profiles for Ra/Rb = 2.5, 3, 4, 5, 6, 8, and 10.

Figure 17.12, which presents velocity profiles for different values of Ra/Rb, shows this clearly. As Ra/Rb increases, more and more of the channel begins to flow, and once Ra/Rb is sufficiently large, the velocity profile eventually becomes linear, which is equivalent to that for a Newtonian fluid.

17.5.2 Unit Cavity: Isotropic Model

We now begin to consider nonlinear two-dimensional convection. In this pioneering work, we will adopt the threshold model for flow, rather than the BR2D model, but in the interests of computational ease, this will be regularized using the tanh model, which was discussed earlier. Therefore, the x-momentum equation

$$u = \begin{cases} -\dfrac{K}{\mu}\left[1 - \dfrac{G}{|p_x|}\right] p_x & \text{when } |p_x| > G \\ 0 & \text{otherwise} \end{cases} \tag{17.49}$$

will be replaced by

$$\left[1 + G\frac{K}{\mu}\frac{\tanh(cu)}{u}\right] u = -\frac{K}{\mu} p_x. \tag{17.50}$$

These two equations appeared earlier as Equations 17.9 and 17.13, but are quoted here so that this section is self-contained. We also note that for porous media consisting of channels of width h, the yield pressure gradient is given by Equation 17.17 and is $G = 2\tau_0/h$.

For fully nonlinear convection, the appropriate frame-invariant momentum equations now take the form

$$\left[1 + G\frac{K}{\mu}\frac{\tanh(cq)}{q}\right] u = -\frac{K}{\mu} p_x, \tag{17.51}$$

$$\left[1+G\frac{K}{\mu}\frac{\tanh(cq)}{q}\right]w=-\frac{K}{\mu}\left[p_z-\rho g\beta(T-T_{\text{ref}})\right], \tag{17.52}$$

where $q^2 = u^2 + w^2$. These two equations are supplemented by the equations of continuity and heat transfer:

$$u_x + w_z = 0, \tag{17.53}$$

$$\chi T_t + uT_x + wT_z = \alpha\left(T_{xx} + T_{zz}\right). \tag{17.54}$$

Now we nondimensionalize using the following scalings:

$$(x,z)\to L(x,z),\ \ (u,w)\to\frac{\alpha}{L}(u,w),\ \ \ p\to\frac{\alpha\mu}{K}p,\ \ T\to T_{\text{ref}}+\Delta T\,\theta,\ \ \ c\to\frac{L}{\alpha}c,\ \ \ t\to\chi\frac{L^2}{\alpha}t. \tag{17.55}$$

In this equation, χ is the ratio of the specific heats of the porous medium and the fluid, while L is the height of the cavity. The full set of nondimensional equations that govern the two-dimensional convection of a Bingham fluid in a porous medium is, therefore,

$$u_x + w_z = 0, \tag{17.56}$$

$$\left[1+\text{Rb}\frac{\tanh(cq)}{q}\right]u=-p_x, \tag{17.57}$$

$$\left[1+\text{Rb}\frac{\tanh(cq)}{q}\right]w=-p_z+\text{Ra}\,\theta, \tag{17.58}$$

$$\theta_t + u\theta_x + w\theta_z = \theta_{xx} + \theta_{zz}. \tag{17.59}$$

These four equations may be reduced to two by the introduction of the streamfunction, ψ, defined according to $u = -\psi_z$ and $w = \psi_x$. The equation of continuity is satisfied, while the momentum and heat transport equations reduce to the following forms:

$$\nabla^2\psi+\frac{\text{Rb}\tanh(cq)}{q^3}\left[\psi_z^2\psi_{xx}-2\psi_x\psi_z\psi_{xz}+\psi_x^2\psi_{zz}\right]$$
$$+\frac{\text{Rb}\,c\,\text{sech}^2(cq)}{q^2}\left[\psi_x^2\psi_{xx}+2\psi_x\psi_z\psi_{xz}+\psi_z^2\psi_{zz}\right]=\text{Ra}\theta_x, \tag{17.60}$$

$$\theta_t + \psi_x\theta_z - \psi_z\theta_x = \nabla^2\theta, \tag{17.61}$$

where

$$q=\sqrt{\psi_x^2+\psi_z^2}. \tag{17.62}$$

The cavity is a unit square which lies between −1/2 and 1/2 in the x-direction. The streamfunction is zero on all four boundaries. We set $\theta = \pm\frac{1}{2}$ on $x = \pm\frac{1}{2}$, while $\theta_z = 0$ on both $z = 0$ and $z = 1$. Thus, the upper and lower surfaces are insulated.

We have adopted a very straightforward and quite standard method of discretization where three-point central differences were used to approximate each spatial derivative in Equations 17.60 through 17.62. The Neumann conditions for θ on the upper and lower surfaces use the fictitious point approach described well in Roache (1976) and used frequently by the present author. Steady-state solutions were undertaken using Gauss–Seidel iteration as this was quicker than using an explicit time-stepping method. The author is aware that faster methods exist, and these will be adopted for a more wide-ranging survey of the effects of yield stress on convection. We used 48 equally spaced intervals in each direction—this was a compromise between accuracy and speed of computation. Again, future work with faster methods will also use finer grids and also allow the investigation of cavities with aspect ratios other than unity. In the present computations, we have used $c = 3$ in the tanh profile.

Figure 17.13 shows the streamlines (continuous) and isotherms (dashed) for six cases where Ra = 100. The values of Rb are 0, 5, 10, 15, 20, and 25. The value, Rb = 0, corresponds to a Newtonian fluid without a yield stress. At this value of Ra, boundary layers on the vertical walls are only just beginning to become distinct. Flow is quite rapid near the base of the hot wall, as is inferred by the closeness of the streamlines and also near the top of the cold wall. At this value of Ra, there is quite a strong deformation of the isotherms from the vertical orientation that they have when Ra = 0 and which corresponds to a conduction solution.

As Rb increases, first to 5 and then to 10, we see an increasingly large central region that, if one were using a threshold gradient model, would correspond to a stagnant region. Here there is

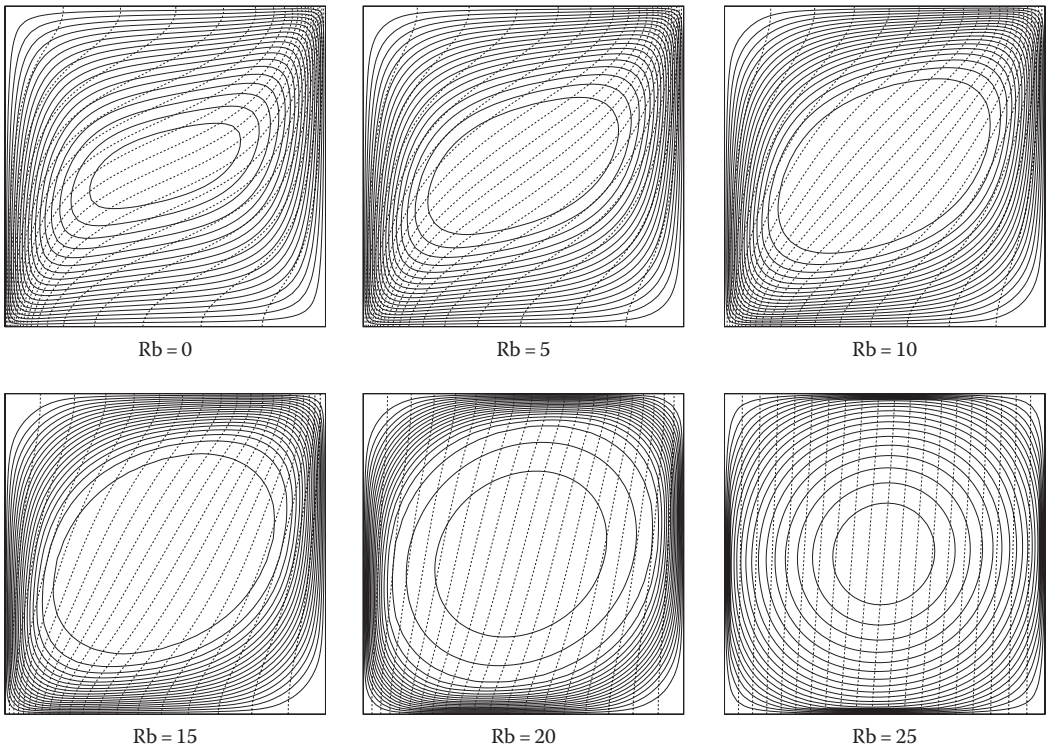

FIGURE 17.13 Streamlines (continuous) and isotherms (dashed) for $c = 3$ and Ra = 100 using an isotropic model.

very slow flow. Although the boundary layers near the vertical wall appear more distinctly, the overall circulation of fluid has decreased as Rb has increased, and this may also be inferred by the decreasing deformation of the isotherms. At still higher values of Rb, flow tends to be confined to a racetrack-like circuit mainly near the four straight boundaries, which is reminiscent of the network analysis in Section 17.4. As Rb increases, the width of the racetrack decreases. When Rb = 25, the overall flow is quite weak, and the isotherms are almost vertical. In this case, the racetrack is very narrow indeed, and a further slight increase in Rb would cause the flow to stop. The concentric streamlines that appear here reflect the fact that $c = 3$; fewer streamlines will appear in the central region when c takes larger values.

We summarize a more extensive set of computations in Figure 17.14. This figure shows the variation of both $|\psi|_{\max}$ and the Nusselt number with Ra for various values of Rb. Here we define the Nusselt number as

$$\mathrm{Nu} = -\int_0^1 \frac{\partial \theta}{\partial x}\, dy, \tag{17.63}$$

at either $x = 0$ or $x = 1$. Although the derivative is evaluated using a one-sided finite difference approximation, the value obtained may be shown to be of second-order accuracy, and the integral is performed using the trapezium rule. When Ra = 0, the conduction solution prevails, and Nu = 1.

When Rb = 0, we see both $|\psi|_{\max}$ and Nu increasing with Ra. When Rb takes nonzero values, both these quantities rise very slowly as Ra increases from zero due to the high apparent viscosity for such small buoyancy forces; see Equation 17.58. This rise becomes even more sedate as c increases. A more rapid rise then ensues once the yield threshold has been passed, and once more, it is necessary to point out that larger values of c will show the transition from slow growth to a rapid ascent increasingly clearly. The effect of increasing values of Rb is seen quite clearly in this figure, and one

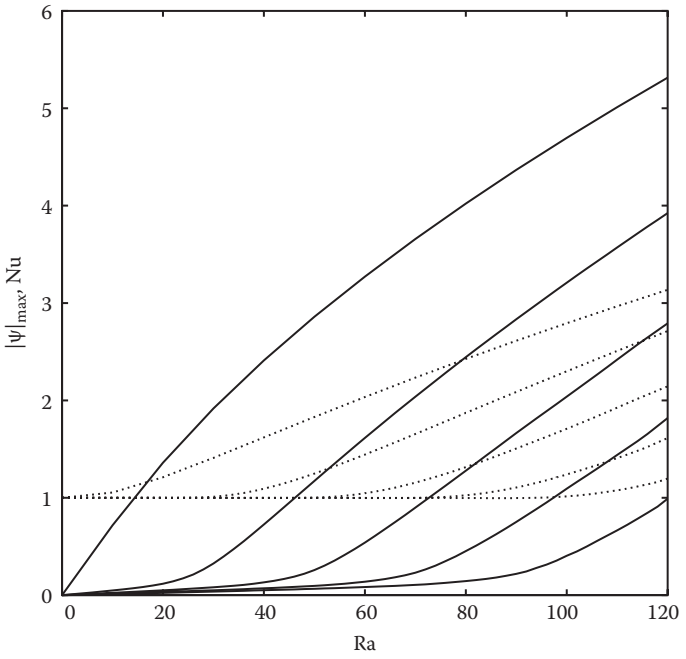

FIGURE 17.14 Variation of $|\psi|_{\max}$ (continuous) and Nu (dashed) with Ra for Rb = 0, 5, 10, 15, and 20. The value $c = 3$ was used.

may extrapolate easily to higher values of both Rb and Ra, at least in a qualitative sense. Finally, we note that the variations in $|\psi|_{\max}$ and Nu are consistent with the earlier network analysis, which gives Ra = 4Rb as being the value above which flow begins to ensue.

17.5.3 Unit Cavity: Anisotropic Model

We now consider a Darcy–Bingham model which displays the characteristics that were found in the network analysis of Section 17.4. If the porous medium is composed solely of equally spaced vertical and horizontal channels, then it is clear that flow in, say, the z-direction at one point will not affect the flow in the x-direction. Therefore, we may replace Equations 17.57 and 17.58 by

$$\left[1 + \mathrm{Rb}\,\frac{\tanh(cu)}{u}\right] u = -p_x, \tag{17.64}$$

$$\left[1 + \mathrm{Rb}\,\frac{\tanh(cw)}{w}\right] w = -p_z + \mathrm{Ra}\,\theta. \tag{17.65}$$

These may be simplified to the forms

$$u + \mathrm{Rb}\tanh(cu) = -p_x, \tag{17.66}$$

$$w + \mathrm{Rb}\tanh(cw) = -p_z + \mathrm{Ra}\,\theta. \tag{17.67}$$

Introduction of the streamfunction as before yields the following momentum equation:

$$\left[1 + \mathrm{Rb}\,c\,\mathrm{sech}^2(c\psi_x)\right]\psi_{xx} + \left[1 + \mathrm{Rb}\,c\,\mathrm{sech}^2(c\psi_z)\right]\psi_{zz} = \mathrm{Ra}\,\theta_x, \tag{17.68}$$

while the heat transport equation is unchanged. This new system of equations was solved in an identical manner to those in the previous subsection.

Figure 17.15 shows how the streamlines and isotherms vary as Rb increases where $c = 3$ and Ra = 100 have been taken. Superficially, these contour plots look very much like those for the isotropic model, but there is a difference. At intermediate values of Rb, such as the range from 10 to 20 for the present value of the Rayleigh number, the racetrack path of the streamlines is now confined to regions very close to the bounding surfaces where the flow is essentially either vertical or horizontal, the flow turns close to the corners, and the region in which flow takes place is narrower. There is little change in the isotherms.

For the sake of brevity, we do not include a figure that corresponds to Figure 17.14, as it takes an identical qualitative form, and the quantitative data are very similar.

Now we turn to the case of a porous medium where the network of channels is aligned at an angle α to the coordinate directions. Equations 17.66 and 17.67 correspond to $\alpha = 0$, and their modified form to account for an oblique network is

$$u + \mathrm{Rb}\left[\cos\alpha\tanh c(u\cos\alpha + w\sin\alpha) - \sin\alpha\tanh c(w\cos\alpha - u\sin\alpha)\right] = -p_x, \tag{17.69}$$

$$w + \mathrm{Rb}\left[\sin\alpha\tanh c(u\cos\alpha + w\sin\alpha) + \cos\alpha\tanh c(w\cos\alpha - u\sin\alpha)\right] = -p_z + \mathrm{Ra}\,\theta. \tag{17.70}$$

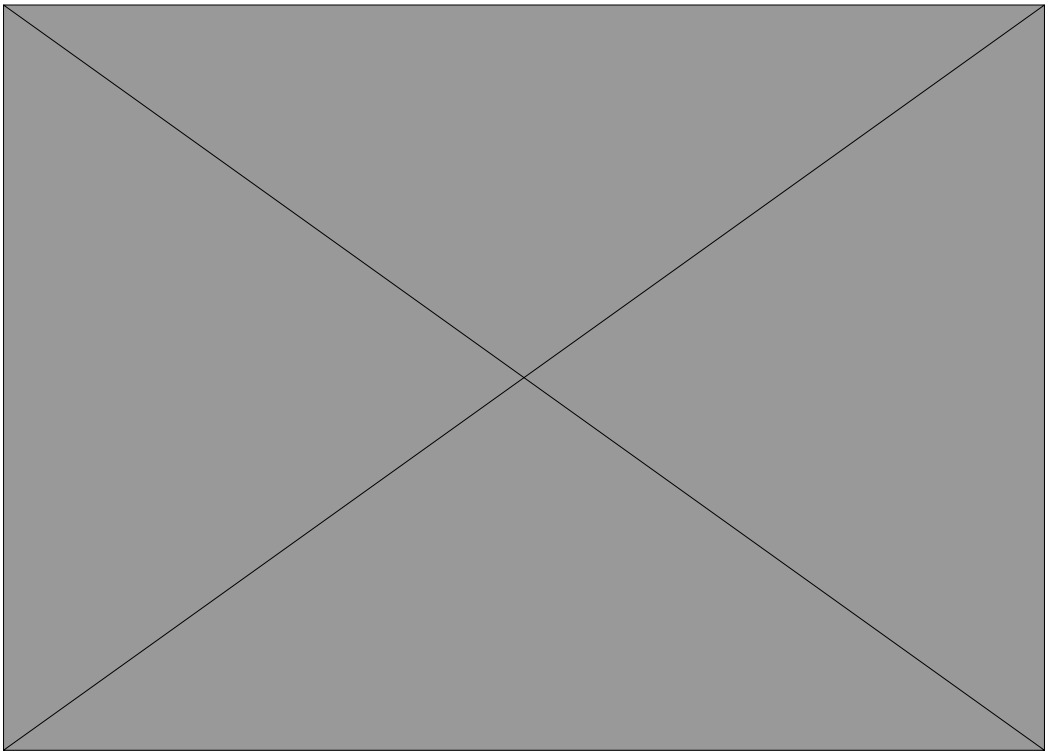

FIGURE 17.15 Streamlines (continuous) and isotherms (dashed) for $c = 3$ and Ra = 100 using a square-network-based anisotropic model.

In terms of the streamfunction, this more complicated pair of equations becomes

$$\nabla^2\psi + \mathrm{Rb}\, c\left[\psi_{xx}\sin^2\alpha - 2\psi_{xz}\sin\alpha\cos\alpha + \psi_{zz}\cos^2\alpha\right]\mathrm{sech}^2 c(\psi_x\sin\alpha - \psi_z\cos\alpha)$$
$$+\mathrm{Rb}\, c\left[\psi_{xx}\cos^2\alpha + 2\psi_{xz}\sin\alpha\cos\alpha + \psi_{zz}\sin^2\alpha\right]\mathrm{sech}^2 c(\psi_x\cos\alpha + \psi_z\sin\alpha) = \mathrm{Ra}\,\theta_x, \tag{17.71}$$

where the heat transport equation is again unchanged.

Figure 17.16 shows six sets of streamlines and isotherms for different values of Rb when Ra = 100, $c = 3$, and $\alpha = 45°$. We see that, even when Rb is as small as 5, the orientation of the microchannels is very evident in the pattern of the streamlines. There are now quite pronounced dead zones in the top left and bottom right corners, where it is very difficult for the fluid to penetrate because of the microstructure. As Rb increases, the racetrack pattern evolves once more, taking its clearest form when Rb = 15. The flow has become very weak when Rb = 20 with only a hint of strong flow near the central portions of each of the four walls. Convection is almost nonexistent when Rb = 25, and the case lies well within the high-viscosity zone of the tanh model. At this point, the isotherms have deformed only slightly from the vertical.

Figure 17.17 shows the effect of varying α on the flow pattern for the case $c = 3$, Rb = 10, and Ra = 100. For these values of Rb and Ra, the flow is quite strong, and there is a large, essentially unyielded, zone in the center of the cavity. The orientation of the underlying network is very evident indeed in the computed streamlines. As α increases from zero, the natural path for the flow near the hot left surface becomes increasingly misaligned with the direction of the buoyancy force, and

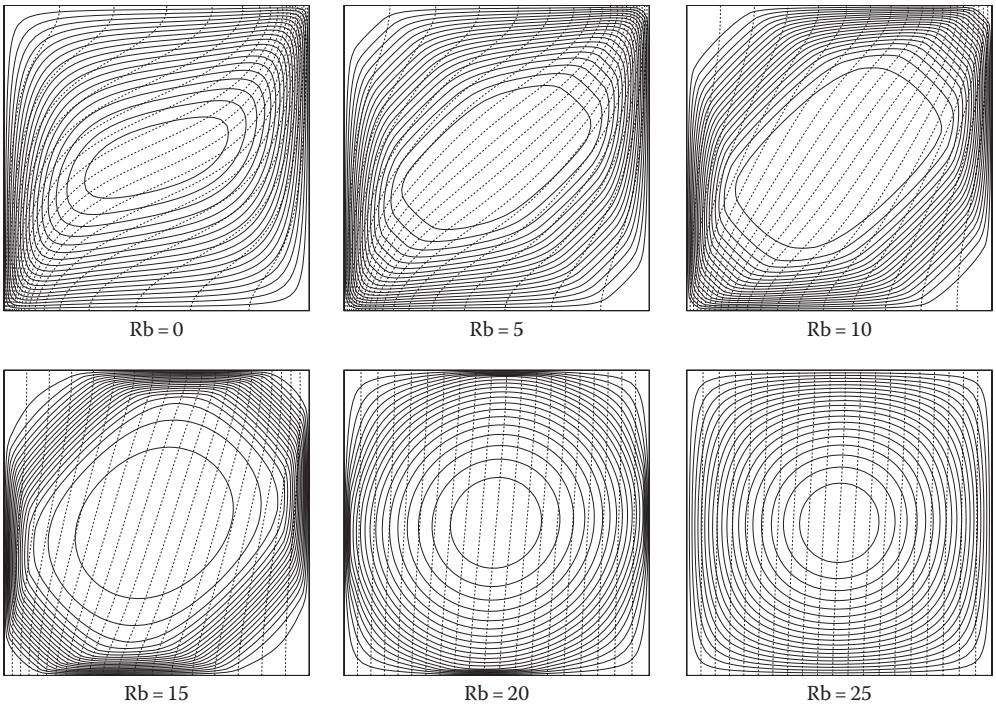

FIGURE 17.16 Streamlines (continuous) and isotherms (dashed) for $c = 3$ and Ra = 100 using a square-network-based anisotropic model with $\alpha = 45°$.

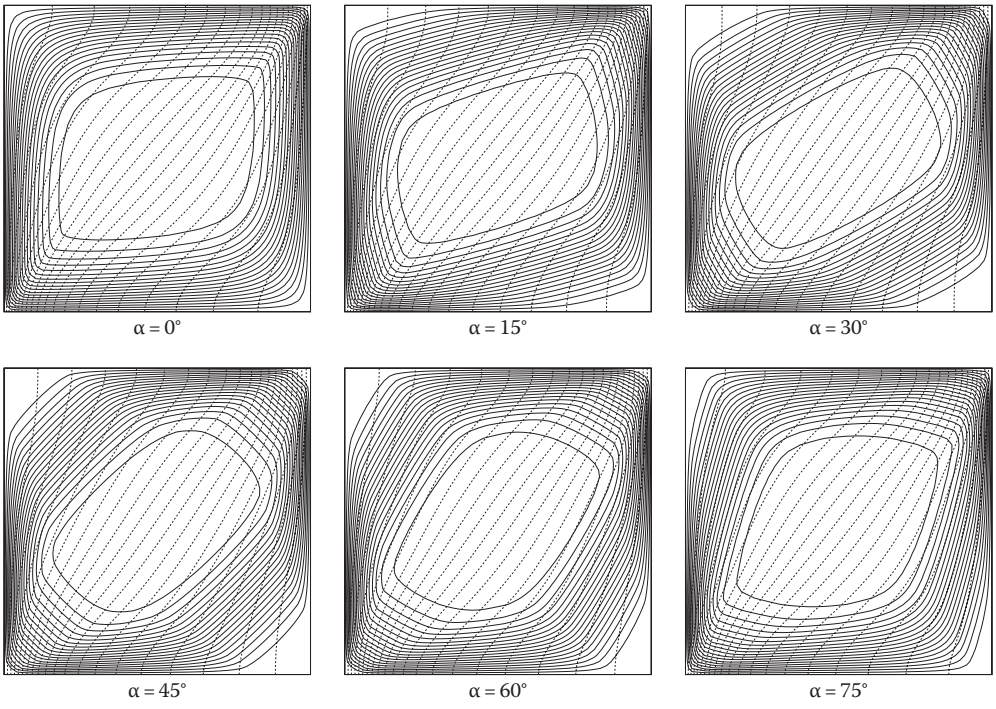

FIGURE 17.17 Streamlines (continuous) and isotherms (dashed) for Rb = 10, $c = 3$, and Ra = 100 using a square-network-based anisotropic model with different values of α.

therefore buoyancy becomes less effective to move the fluid. Therefore, there is a weakening of the flow and a reduction in the heat transfer across the layer. That this is so may be seen by the movement of the top of the leftmost isotherm as α increases from zero. When α approaches 90°, a case that is identical to $\alpha = 0°$, then the flow strengthens once more.

Finally, it is worth saying that the double glazing problem in porous media is one where, for a Newtonian fluid without a yield stress, all that happens as Ra increases is that the flow gets stronger and the rate of heat transfer across the layer increases. There is no instability that will occur, and the thermal boundary layers on the sidewalls become thinner. Indeed, even for a vertical channel, the studies of Gill (1969) and Lewis et al. (1995) have shown that instability does not happen when the flow is governed by Darcy's law. We suspect strongly that this property will also be shared by a convecting Bingham fluid.

17.6 DARCY–BÉNARD CONVECTION

We now consider the convection of a Bingham fluid in a horizontal porous layer which is heated from below. This is, in effect, the double glazing problem rotated through 90° with the hot surface located below the cold one. This generic problem is known by a variety of names: the Darcy–Bénard problem, the porous Bénard problem, the Lapwood problem, and the Horton and Rogers problem, with occasional merging between names, such as the HRL or Horton–Rogers–Lapwood problem. The various names that appear here were the pioneers, and the papers by Horton and Rogers (1945) and Lapwood (1948) are considered to be the founding works. It is these authors who determined that, for a Newtonian fluid, convection arises first when the Rayleigh number reaches $4\pi^2$ and the wavenumber is equal to π. Thus, the convection cells which appear first as Ra increases have a precisely square cross section. In this section, we present some very preliminary computations for what we shall call the Darcy–Bingham–Bénard problem. In view of the fact that the first cell to appear as Ra increases has unit aspect ratio, we will confine our studies for now to the same unit square that was the subject of the previous section. Our primary interest is to see how the presence of a yield stress alters the classical onset behavior, namely, a supercritical bifurcation to strongly convecting flow. Our numerical simulations were undertaken in an identical way and with the same precautions as were used for the sidewall-heated cavity. The only difference was that the Gauss–Seidel iterations were initiated using a strongly perturbed temperature field.

Figure 17.18 shows a comparison between the various types of Darcy–Bingham models for the case Ra = 200, with $c = 10$, and Rb = 12. In Figure 17.18, we compare the flow of a Newtonian fluid with the isotropic Darcy–Bingham model and the anisotropic models with $\alpha = 0°$ and $\alpha = 45°$. We have chosen to use the parameter values, Ra = 200, $c = 10$, and Rb = 12, in order to show clearly the essential differences in the resulting flow pattern between these models; other parameter sets tend not to be so clear.

For the Newtonian fluid, Ra = 200 is well into the nonlinear regime and represents a value which is very close to five times the critical value. This steady flow is very strong, and the isotherms have been deformed into a very clear S-shape by the power of the flow. It is very noticeable that the three Darcy–Bingham models have isotherms that are less deformed than for the Newtonian fluid due to the flow being weaker as it had to overcome the yield threshold.

The nature of each of the Darcy–Bingham models is particularly evident when looking at the streamlines. The isotropic model has streamlines which follow a racetrack pattern that is quite round, and the flow tends to avoid the downstream corners on the vertical surfaces. On the other hand, the anisotropic model yields streamline patterns which follow quite closely the imposed direction of the underlying network with relatively sharp "corners" when the fluid has to turn.

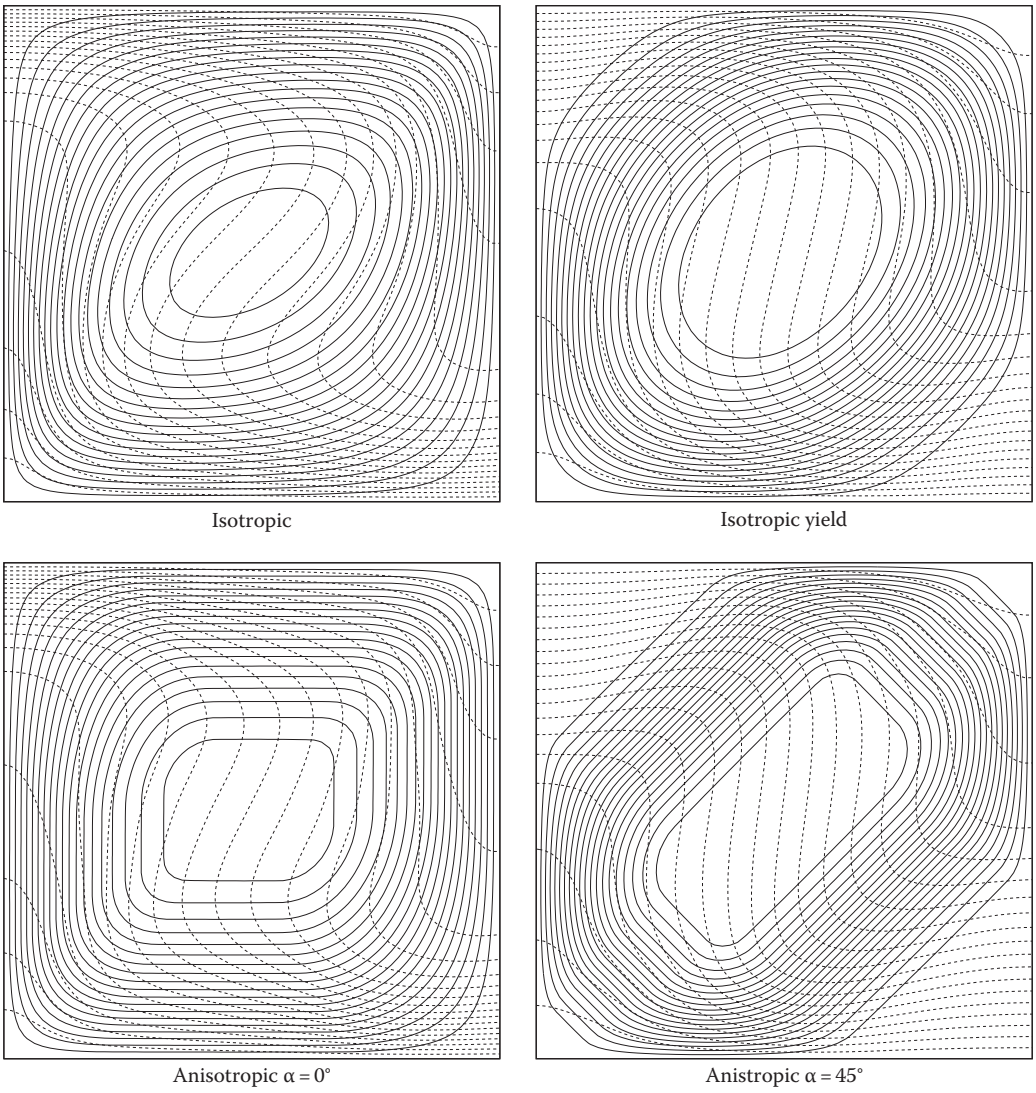

FIGURE 17.18 Comparing four Darcy–Bingham models for Ra = 200, Rb = 12, and $c = 10$.

The usual first step when considering a flow with convective instability is to undertake a linear stability analysis. This involves perturbing the quiescent basic state with a disturbance of small amplitude. For Darcy–Bingham flows, such a disturbance will not overcome the yield threshold, and therefore such a configuration is stable to all small-amplitude disturbances. If, however, one considers the tanh model regularization of the Darcy–Bingham law, then given that the effective viscosity is $(1 + \mathrm{Rb}\, c)$ times the true viscosity when the flow is slow, a linear stability analysis will yield a value of $4\pi^2(1 + \mathrm{Rb}\, c)$ for onset. For the isotropic yield case considered earlier, this means that the critical Rayleigh number is $484\pi^2$, which is well above the value of 200 which was used. So at this juncture, it would seem logical to assume that the point of linear instability represents a subcritical bifurcation given that we have already computed flows at a much lower value of Ra; this facet is presently being studied in detail.

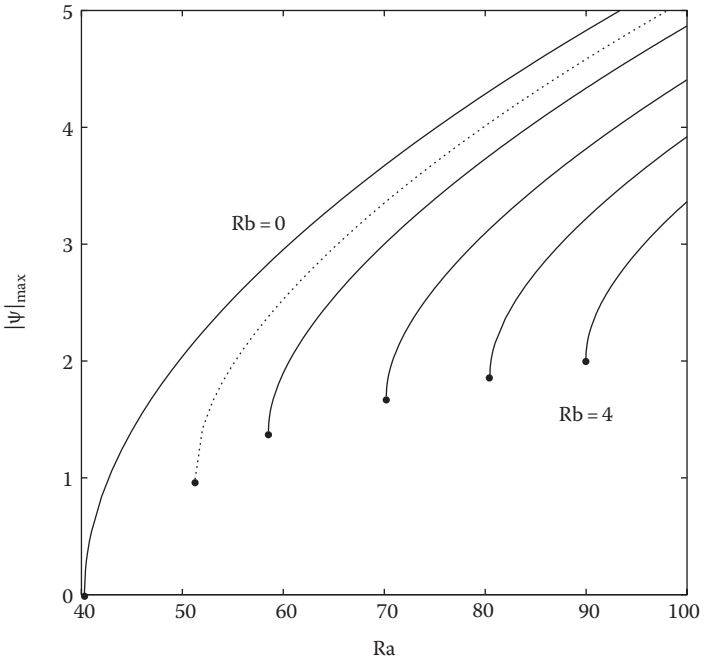

FIGURE 17.19 Variation of $|\psi|_{max}$ with Ra for $c = 3$ and for Rb = 0, 0.5 (dashed), 1, 2, 3, and 4. Turning points, which represent the nonlinear onset of convection, are shown as black disks.

In Figure 17.19, we show the variation of $|\psi|_{max}$ with Ra when $c = 3$ and for selected values of Rb. Apart from when Rb = 0, which represents a Newtonian fluid, all these solution curves have a turning point at a nonzero value of $|\psi|_{max.}$ A different type of solver to the one used here would be necessary to compute beyond the turning point since this branch of solutions is expected to join up with the point of linear instability due to the present adoption of the tanh model for the computations. But for now, we may at least conclude that we are able to find steady convecting solutions for the Darcy–Bingham–Bénard convection although it was necessary to introduce a large perturbation in order to be able to compute them. As will be expected, the solution curves tend toward that of the Newtonian fluid as Rb → 0.

17.7 CONVECTIVE BOUNDARY-LAYER FLOWS OF A BINGHAM FLUID

In this final section, we will consider an unsteady boundary-layer flow and comment on certain aspects of steady boundary-layer flows in an infinite domain.

17.7.1 Unsteady Boundary-Layer Flow

The problem that we will solve in detail here is the consequence of suddenly raising the temperature of a vertical surface which bounds a porous medium to a new constant value. It is well known that the temperature field conducts inward with a complementary error function profile and that buoyancy forces then cause a unidirectional flow. Therefore, no entrainment into the boundary layer occurs because the induced flow is parallel to the heated surface. This will be considered for two different cases: (1) where the flow domain is infinite in extent and (2) where there is a second cold boundary that is parallel to the hot one. We note that the coordinate directions are defined in the traditional way for boundary layers, namely, that x represents the streamwise direction, which is vertical here. The coordinate z represents the cross-stream direction, that is, the horizontal direction.

17.7.1.1 Infinite Domain

We will adopt momentum equations which are the appropriate modification of the threshold model given in Equation 17.9, which account for buoyancy. These will be in nondimensional form, and we will adopt the standard convention for boundary-layer flows that the heated surface is always in the x-direction. The full governing equations are, therefore,

$$\bar{u}_{\bar{x}} + \bar{w}_{\bar{z}} = 0, \tag{17.72}$$

$$\bar{u} = \begin{cases} \left[1 - \dfrac{\mathrm{Rb}}{\sqrt{(\mathrm{Ra}\,\theta - \bar{p}_{\bar{x}})^2 + \bar{p}_{\bar{z}}^2}}\right]\left(\mathrm{Ra}\,\theta - \bar{p}_{\bar{x}}\right) & \text{when } \sqrt{(\mathrm{Ra}\,\theta - \bar{p}_{\bar{x}})^2 + \bar{p}_{\bar{z}}^2} > \mathrm{Rb}, \\ 0 & \text{otherwise}, \end{cases} \tag{17.73}$$

$$\bar{w} = \begin{cases} -\left[1 - \dfrac{\mathrm{Rb}}{\sqrt{(\mathrm{Ra}\,\theta - \bar{p}_{\bar{x}})^2 + \bar{p}_{\bar{z}}^2}}\right]\bar{p}_{\bar{z}} & \text{when } \sqrt{(\mathrm{Ra}\,\theta - \bar{p}_{\bar{x}})^2 + \bar{p}_{\bar{z}}^2} > \mathrm{Rb}, \\ 0 & \text{otherwise}, \end{cases} \tag{17.74}$$

and

$$\theta_{\bar{t}} + \bar{u}\theta_{\bar{x}} + \bar{w}\theta_{\bar{z}} = \theta_{\bar{x}\bar{x}} + \theta_{\bar{z}\bar{z}}, \tag{17.75}$$

where Rb is the yield threshold. The initial condition is that $\theta = 0$ everywhere, but that $\theta = 1$ on the vertical boundary at $\bar{z} = 0$. The domain is doubly infinite in the x-direction, and therefore there is no x-dependence. We may therefore set $\bar{w} = 0$ and $\bar{p}_{\bar{z}} = 0$, and let both $\bar{u}$ and θ be functions of $\bar{z}$ and t. The equation of continuity is satisfied, and therefore only the $\bar{x}$-momentum and heat transport equations need to be solved.

A rescaling is introduced:

$$\bar{u} = \mathrm{Ra}\,u, \quad \bar{x} = x, \quad \bar{z} = z, \quad \bar{t} = t, \quad \bar{p} = p, \quad \mathrm{Rb} = \mathrm{Ra}\,B, \tag{17.76}$$

and therefore we need to solve

$$u = \begin{cases} \theta - p_x - B & \text{when } B < \theta - p_x \\ 0 & \text{when } -B < \theta - p_x < B \\ \theta - p_x + B & \text{when } \theta - p_x < -B, \end{cases} \tag{17.77}$$

and

$$\theta_t = \theta_{zz}. \tag{17.78}$$

The solution for θ is

$$\theta = \mathrm{erfc}\,\eta = \frac{2}{\sqrt{\pi}}\int_{\eta}^{\infty} e^{-\xi^2}\,d\xi, \tag{17.79}$$

where $\eta = z/2\sqrt{t}$.

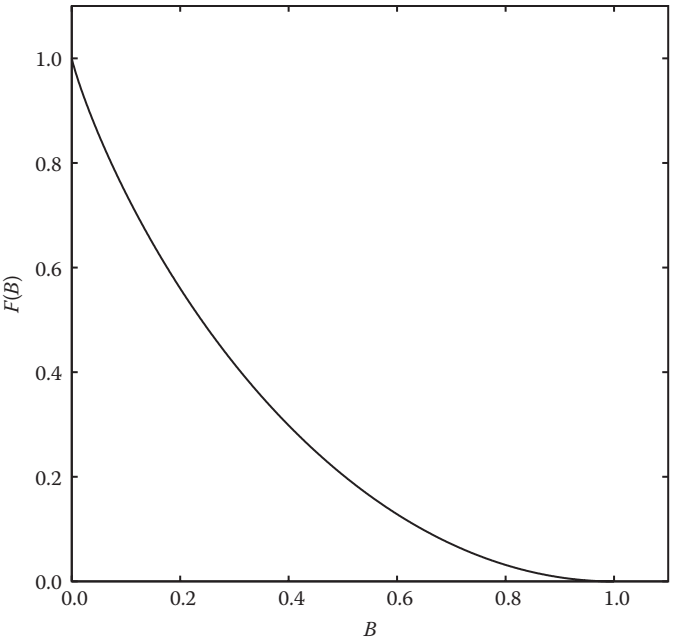

FIGURE 17.20 The function $F(B)$ as given by Equation 17.81.

In this infinite domain, we expect the suddenly heated surface to provide only upward movement of the fluid, and therefore we may set $p_x = 0$. This means that the hydrostatic component of the vertical pressure gradient is precisely that for the ambient fluid at $\theta = 0$. Equation 17.77 simplifies to

$$u = \begin{cases} \theta - B & \text{when } 0 < B < \theta \\ 0 & \text{when } 0 < \theta < B. \end{cases} \tag{17.80}$$

Thus, flow is induced only when $B < 1$ and when B takes larger values then buoyancy provides insufficient body force to cause the fluid to yield.

The total velocity flux may now be found as a function of time and B when $0 < B < 1$. If we define η_B to be where the yield surface is, that is, where erfc $\eta_B = B$, then the velocity flux is

$$Q = \int_0^\infty u\,dz = 2\sqrt{t}\int_0^{\eta_B} (\operatorname{erfc}\xi - B)\,d\xi = \frac{2\sqrt{t}}{\sqrt{\pi}}(1 - e^{-\eta_B^2}) \equiv \frac{2\sqrt{t}}{\sqrt{\pi}}F(B). \tag{17.81}$$

The variation of $F(B)$ is given in Figure 17.20, for reference, and we see how this scaled velocity flux decreases toward zero as $B \to 1$. Therefore, we conclude that free convective boundary-layer flow is possible for the suddenly heated problem in an infinite domain provided that $B < 1$ or equivalently that Rb < Ra.

17.7.1.2 Tall Cavity

We now consider a tall cavity or, equivalently, a cavity of finite width that is very tall. For this finite but tall cavity, the flow field well away from the upper and lower ends will be unidirectional and therefore independent of x, but the presence of the upper and lower surfaces means that there will necessarily be an overall zero mass flux up the layer, in contrast to the infinite domain case just considered.

Equation 17.78 will be solved subject to $\theta = 1$ at $z = 0$ and $\theta = 0$ at $z = 1$ with $\theta = 0$ at $t = 0$. Using Laplace Transforms, we find that

$$\theta = \sum_{n=0}^{\infty} \left[\operatorname{erfc}\left(\eta + \frac{n}{\sqrt{t}} \right) - \operatorname{erfc}\left(\frac{n+1}{\sqrt{t}} - \eta \right) \right]. \tag{17.82}$$

The temperature field now evolves at least initially according to the complementary error function solution given in Equation 17.79. Subsequently, this growing profile is modified when it encounters the cold boundary at $z = 1$, and it eventually attains the steady linear profile given by $\theta = 1 - z$.

As the temperature field evolves, we cannot allow p_x in Equation 17.77 to remain zero. It has to change in time until it takes the value 1/2 as $t \to \infty$; this latter value means that there is no net fluid flux up the layer. At intermediate times, we need to find the value of p_x to ensure an overall zero flux. We also note that there will be an unyielded section in the middle of the evolving temperature field, and if these are located at $\eta = \eta_1$ and $\eta = \eta_2$, where $\eta_1 < \eta_2$, then we have

$$\theta(\eta_1, t) = p_x + B \tag{17.83}$$

and

$$\theta(\eta_2, t) = p_x - B. \tag{17.84}$$

Now the zero flux condition is equivalent to

$$I = \int_0^{\eta_3} u \, d\eta = \int_0^{\eta_1} \left[\theta - p_x - B \right] d\eta + \int_{\eta_2}^{\eta_3} \left[\theta - p_x + B \right] d\eta. \tag{17.85}$$

It is possible to proceed analytically with this, and we obtain

$$\begin{aligned}
I = {} & p_x(-\eta_1 + \eta_2 - \eta_3) + B(-\eta_1 - \eta_2 + \eta_3) \\
& + \frac{1}{\sqrt{\pi}} \sum_{n=0}^{\infty} \left[e^{-[\eta_0 + n/\sqrt{t}]^2} + e^{-[(n+1)/\sqrt{t} - \eta_0]^2} - e^{-[\eta_1 + n/\sqrt{t}]^2} + e^{-[(n+1)/\sqrt{t} - \eta_1]^2} \right] \\
& + \frac{1}{\sqrt{\pi}} \sum_{n=0}^{\infty} \left[e^{-[\eta_2 + n/\sqrt{t}]^2} + e^{-[(n+1)/\sqrt{t} - \eta_2]^2} - e^{-[\eta_3 + n/\sqrt{t}]^2} + e^{-[(n+1)/\sqrt{t} - \eta_3]^2} \right] \\
& - \sum_{n=0}^{\infty} \left[\left(\eta_0 + n/\sqrt{t} \right) \operatorname{erfc}\left(\eta_0 + n/\sqrt{t} \right) + \left((n+1)/\sqrt{t} - \eta_0 \right) \operatorname{erfc}\left((n+1)/\sqrt{t} - \eta_0 \right) \right] \\
& + \sum_{n=0}^{\infty} \left[\left(\eta_1 + n/\sqrt{t} \right) \operatorname{erfc}\left(\eta_1 + n/\sqrt{t} \right) + \left((n+1)/\sqrt{t} - \eta_1 \right) \operatorname{erfc}\left((n+1)/\sqrt{t} - \eta_1 \right) \right] \\
& - \sum_{n=0}^{\infty} \left[\left(\eta_2 + n/\sqrt{t} \right) \operatorname{erfc}\left(\eta_2 + n/\sqrt{t} \right) + \left((n+1)/\sqrt{t} - \eta_2 \right) \operatorname{erfc}\left((n+1)/\sqrt{t} - \eta_2 \right) \right] \\
& + \sum_{n=0}^{\infty} \left[\left(\eta_3 + n/\sqrt{t} \right) \operatorname{erfc}\left(\eta_3 + n/\sqrt{t} \right) + \left((n+1)/\sqrt{t} - \eta_3 \right) \operatorname{erfc}\left((n+1)/\sqrt{t} - \eta_3 \right) \right]
\end{aligned} \tag{17.86}$$

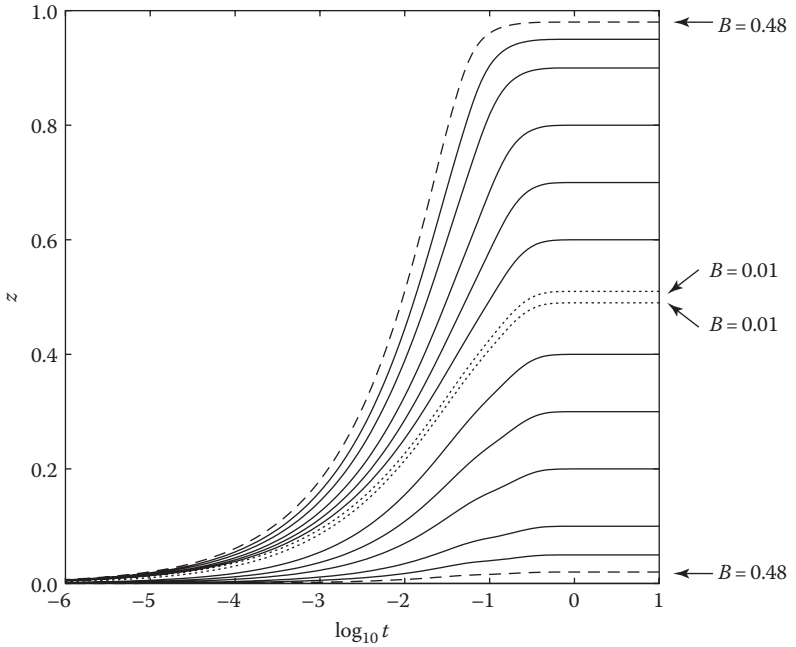

FIGURE 17.21 Displaying where the yield surfaces are used as a function of time for $B = 0.01$ (dotted lines) 0.1, 0.2, 0.3, 0.4, 0.45, and 0.48 (dashed lines). Each value of B has two yield surfaces, and the fluid is stationary between these surfaces.

where $I = 0$. Here we have used $\eta_0 = 0$ and $\eta_3 = 1/2\sqrt{t}$ (i.e., $y = 1$) to make the above formula more easily readable. Therefore, we have three equations to solve for η_1, η_2, and p_x. A straightforward multidimensional Newton–Raphson scheme was used to find these values.

Figure 17.21 shows where the two yield surfaces are as a function of time. At early times, the thermal boundary layer is thin, and therefore the yield surfaces are also close to the heated surface. But as the boundary layer thickens, the yield surfaces move away from the hot surface and eventually become located at equal distances either side of $y = ½$. We also note that the width of the unyielded zone remains small when B is small, but it eventually fills the whole channel as $B \to ½$. This represents the maximum value of B for which flow will arise and should be contrasted with $B = 1$ for the infinite domain.

Figure 17.22 shows how p_x evolves with time. At large times, the temperature field has reached a steady state, and we have already noted that an overall zero fluid flux corresponds to $p_x = ½$. This value of p_x is equivalent to changing the reference temperature from zero, the cold boundary temperature, to ½, which is the mean temperature of the two walls. At early times, p_x is very slightly above the value of B; given the form of Equation 17.77 (third case), this allows for a very small but negative velocity in almost the whole cavity, and this balances a relatively strong upward flow in the very thin thermal boundary layer near $y = 0$. Then, as time progresses, p_x adjusts toward the value ½.

17.7.2 Comment on Steady Boundary-Layer Flows

The reader will have noticed that while there have been references to many papers in the chapter so far, almost none has been to papers on the effect of a yield stress on convective flows. However, there are 13 papers on boundary-layer flows. Apart from Pascal (1981) and Wang and Tu (1989), these tend to be quite complicated because of the inclusion of many different effects. Thus, Cheng

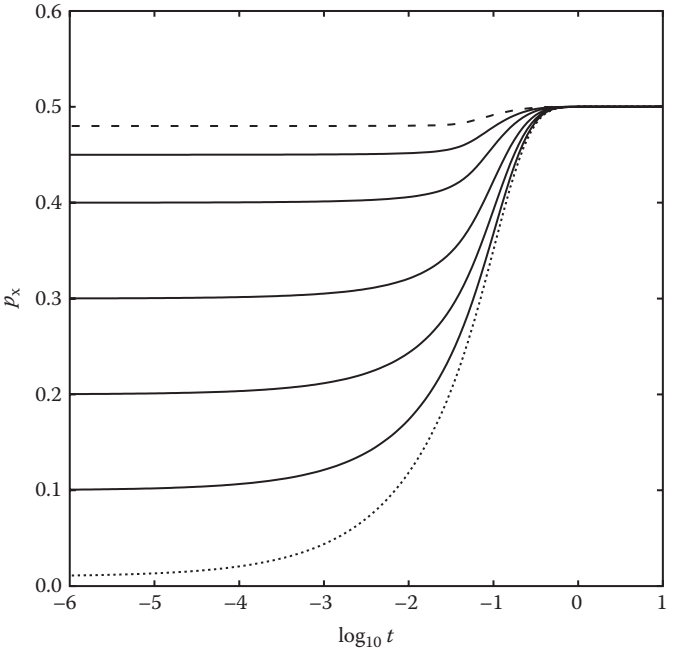

FIGURE 17.22 Displaying the variation with time of the value of p_x, for $B = 0.01$ (dotted line) 0.1, 0.2, 0.3, 0.4, 0.45, and 0.48 (dashed line).

(2006) considers the effect of a variable wall temperature, while Cheng (2011) also includes mass flux. Others who have studied double-diffusive effects are Jumah and Mujumdar (2000, 2001) and Lakshmi Narayana et al. (2009). Ibrahim et al. (2010) consider chemical reactions, while Hady et al. (2011) study nanofluids with a yield stress. Pascal and Pascal (1997) analyze the effect of a lateral mass flux, and Abdel-Gaied and Eid (2011), Wang et al. (2002), and Yang and Wang (1996) all consider boundary layers on axisymmetric bodies.

However, a recent paper by Rees (2015) has sounded a warning note about the general principle of such boundary-layer flows. A common feature of the earlier-quoted papers is that the yield surface lies within the thermal boundary layer. This has a serious consequence when the boundary layer has been formed in a domain of infinite extent. A formal asymptotic theory will involve the limit $\mathrm{Ra} \to \infty$, and for a Newtonian fluid, it is always the case that the induced flow along the heated surface has an asymptotically larger magnitude than the inflow velocity, which is caused by entrainment. Entrainment from the region outside of the boundary layer must happen in order to replenish the upward-moving fluid and to bring cold fluid toward the hot surface in order to inhibit heat conduction into the external domain. For a Bingham fluid with a yield surface within the thermal boundary layer, this entrainment cannot happen, and therefore the computed boundary layer cannot exist.

Rees (2015) also considers in detail what happens when a strict yield threshold is replaced by the tanh law as characterized by the parameter, c, seen earlier. In this case, it is possible to find the induced external circulation, but when the yield threshold model is approached by letting $c \to \infty$, the external pressure gradient also becomes infinite. This confirms the order-of-magnitude argument given in the previous paragraph.

Thus, we need to be very careful when considering thermal boundary-layer flows because the effect on the external environment must also be considered. It is important to mention that certain types of mixed convection problem are exempt from these restrictions. The lateral flux problem considered by Pascal and Pascal (1997) is such that the surface suction at the heated surface will

have already caused the yield threshold to be exceeded, and therefore the upward free convection component merely pushes the overall body force further from the threshold. The same argument will also apply to mixed convection where there is an aiding external flow.

REFERENCES

Abdel-Gaied, S.M., Eid, M.R.: Natural convection of non-Newtonian power-law fluid over axisymmetric and two-dimensional bodies of arbitrary shape in fluid-saturated porous media. *Applied Mathematics and Mechanics*—English Edition **32** (2), 179–188 (2011).

Balhoff, M.T., Thompson, K.E.: Modeling the steady flow of yield-stress fluids in packed beds. *American Institute of Chemical Engineers Journal* **50**, 3034–3048 (2004).

Barnes, H.A.: The yield stress—A review or 'παντα ρει'—Everything flows? *Journal of Non-Newtonian Fluid Mechanics* **81**, 133–178 (1999).

Barnes, H.A., Walters, K.: The yield stress myth. *Rheologica Acta* **24**, 323–326 (1985).

Bayazitoglu, Y., Paslay, P.R., Cernocky, P.: Laminar Bingham fluid flow between vertical parallel plates. *International Journal of Thermal Sciences* **46**, 349–357 (2007).

Cheng, C.-Y.: Natural convection heat and mass transfer of non-Newtonian power law fluids with yield stress in porous media from a vertical plate with variable wall heat and mass fluxes. *International Communications in Heat and Mass Transfer* **33** (9), 1156–1164 (2006).

Cheng, C.-Y.: Soret and Dufour effects on free convection boundary layers of non-Newtonian power law fluids with yield stress in porous media over a vertical plate with variable wall heat and mass fluxes. *International Communications in Heat and Mass Transfer* **38** (5), 615–619 (2011).

Cheng, D.C.-H.: Yield stress: A time-dependent property and how to measure it. *Rheologica Acta* **25**, 542–554 (1986).

Denn, M.M., Bonn, D.: Issues in the flow of yield-stress fluids. *Rheologica Acta* **50**, 307–315 (2011).

Gill, A.E.: A proof that convection in a porous vertical slab is stable. *Journal of Fluid Mechanics* **35**, 545–547 (1969).

Hady, F.M., Ibrahim, F.S., Abdel-Gaied, S.M., Eid, M.R.: Influence of yield stress on free convective boundary-layer flow of a non-Newtonian nanofluid past a vertical plate in a porous medium. *Journal of Mechanical Science and Technology* **25** (8), 2043–2050 (2011).

Horton, C.W., Rogers, F.T. Jr.: Convection currents in a porous medium. *Journal of Applied Physics* **16**, 367–370 (1945).

Ibrahim, F.S., Hady, F.M., Abdel-Gaied, S.M., Eid, M.R.: Influence of chemical reaction on heat and mass transfer of non-Newtonian fluid with yield stress by free convection from vertical surface in porous medium considering Soret effect. *Applied Mathematics and Mechanics*—English Edition **31** (6), 675–684 (2010).

Jamalud-Din, S.-D., Rees, D.A.S., Reddy, B.V.K., Narasimhan, A.: Prediction of natural convection flow using a network model and numerical simulations inside an enclosure with distributed solid blocks. *Heat and Mass Transfer* **46**, 333–343 (2010).

Jeong, S.W.: Determining the viscosity and yield surface of marine sediments using modified Bingham models. *Geosciences Journal* **17** (3), 241–247 (2013).

Jumah, R.Y., Mujumdar, A.S.: Free convection heat and mass transfer of non-Newtonian power law fluids with yield stress from a vertical flat plate in saturated porous media. *International Communications in Heat and Mass Transfer* **27** (4), 485–494 (2000).

Jumah, R.Y., Mujumdar, A.S.: Natural convection heat and mass transfer from a vertical flat plate with variable wall temperature and concentration to power-law fluids with yield stress in a porous medium. *Chemical Engineering Communications* **185**, 165–182 (2001).

Lakshmi Narayana, P.A., Murthy, P.V.S.N., Postelnicu, A.: Soret and Dufour effects on free convection of non-Newtonian power law fluids with yield stress from a vertical flat plate in saturated porous media. *Journal of Porous Media* **12** (10), 967–981 (2009).

Lapwood, E.R.: Convection of a fluid in a porous medium. *Proceedings of the Cambridge Philosophical Society* **44**, 508–521 (1948).

Lewis, S., Bassom, A.P., Rees, D.A.S.: The stability of vertical thermal boundary layer flow in a porous medium. *European Journal of Mechanics B: Fluids* **14**, 395–408 (1995).

Liu, H., Wang, J., Xie, Y., Ma, D., Shi, X.: Flow characteristics of heavy oil through porous media. *Energy Sources Part A—Recovery Utilization and Environmental Effects* **34** (1–4), 347–359 (2012).

Maßmeyer, A.: Thermal instabilities in a yield-stress fluid: From the laboratory to the planetary scale. PhD thesis. Université Paris Sud, Orsay, France (2013).

Mendes, P.R.S., Naccache, M.F., Braga, C.V.M., Nieckele, A.O., Ribeiro, F.S.: Flows of Bingham materials through ideal porous media: An experimental and theoretical study. *Journal of the Brazilian Society of Mechanical Engineers* **24** (1), 40–45 (2002).

Nash, S.: Investigating the flow behaviours of Bingham fluids in porous media. Final year MEng project report supervised by Dr. D.A.S.Rees, Department of Mechanical Engineering, University of Bath, Bath, U.K. (2013).

Papanastasiou, T.C.: Flow of materials with yield. *Journal of Rheology* **31**, 385–404 (1987).

Pascal, H.: Nonsteady flow through porous media in the presence of a threshold gradient. *Acta Mechanica* **39**, 207–224 (1981).

Pascal, J.P., Pascal, H.: Free convection in a non-Newtonian fluid saturated porous medium with lateral mass flux. *International Journal of Non-linear Mechanics* **32** (3), 471–482 (1997).

Rees, D.A.S.: On convective boundary layer flows of a Bingham fluid in a porous medium. *International Journal of Heat and Mass Transfer* **82**, 206–217 (2015).

Roache, P.J.: *Computational Fluid Dynamics*. Hermosa, Albuquerque, NM (1976).

Shenoy, A.V.: Non-Newtonian fluid heat transfer. *Advances in Heat Transfer* **24**, 102–190 (1991).

Sochi, T., Blunt, M.J.: Pore-scale network modeling of Ellis and Herschel-Bulkley fluids. *Journal of Petroleum Science and Engineering* **60**, 105–124 (2008).

Steffe, J.F.: *Rheological Methods on Food Process Engineering*. Freeman Press, East Lansing, MI (1992).

Turan, O., Poole, R.J., Chakraborty, N.: Boundary condition effects on natural convection of Bingham fluids in a square enclosure with differentially heated horizontal walls. Paper NC-05. *Proceedings of CHT-12, the Fifth ICHMT Symposium on Advances in Computational Heat Transfer*, University of Bath, Bath, U.K. (July 1–6, 2012).

Wang, C.Y., Tu, C.J.: Boundary-layer flow and heat-transfer of non-Newtonian fluids in porous-media. *International Journal of Heat and Fluid Flow* **10** (2), 160–165 (1989).

Wang, S.C., Chen, C.K., Yang, Y.T.: Natural convection of non-Newtonian fluids through permeable axisymmetric and two-dimensional bodies in a porous medium. *International Journal of Heat and Mass Transfer* **45** (2), 393–408 (2002).

Yang, Y.T., Wang, S.J.: Free convection heat transfer of non-Newtonian fluids over axisymmetric and two-dimensional bodies of arbitrary shape embedded in a fluid-saturated porous medium. *International Journal of Heat and Mass Transfer* **39** (1), 203–210 (1996).